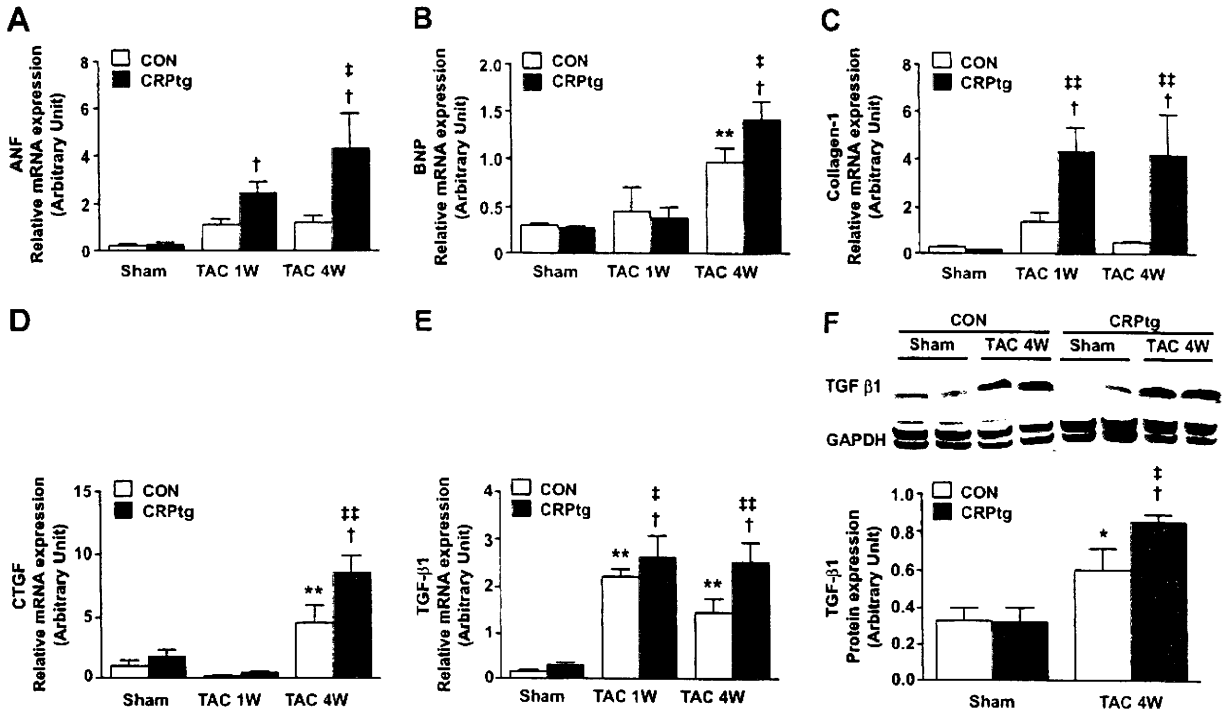

Figure 3. Myocardial expression of hypertrophic and fibrotic markers. Expression of ANF (A), B-type natriuretic peptide (BNP; B), collagen-I (C), connective tissue growth factor (CTGF; D), and TGF-β1 (E) in ventricular tissue. F, Protein expression of TGF-β1 in ventricular tissue of CRPtg and control mice 1 and 4 weeks after TAC or sham operation. *$P<0.05$, **$P<0.01$ vs Sham/CON; †$P<0.01$ vs Sham/CRPtg; ‡$P<0.05$, ‡‡$P<0.01$ vs TAC/CON. 1W indicates 1 week; 4W, 4 weeks.

vated in TAC/CRPtg compared to that in TAC/CON, peaking at 1 week after TAC operation (Figure S2A). NO and iNOS expression were significantly decreased in TAC/CRPtg compared to TAC/CON at both 1 and 4 weeks after TAC operation (Figure S2B).

Macrophage Infiltration and Nuclear Factor-κB/p65 Activation in Cardiomyocytes

Immunohistochemical staining showed an increase in the number of infiltrating Mac-2–positive macrophages in TAC/CRPtg compared to TAC/CON or Sham/CRPtg, peaking 1 week after TAC operation (Figure 5A and 5B). Myocardial CD68 expression 1 week after operation was increased in TAC-operated mice compared to sham-operated mice. TAC/CRPtg mice had higher CD68 expression 1 week after operation compared to TAC/CON.

The number of nuclear localization of phosphorylated nuclear factor-κB (NF-κB)/p65 (p-p65)-positive cardiomyocytes was higher in TAC/CRPtg than in sham-operated mice or TAC/CON 1 week after operation, and it remained elevated 4 weeks after operation in TAC/CRPtg compared to TAC/CON (Figure 6A and 6B). In addition, EMSA demonstrated that nuclear NF-κB-DNA–binding activity was significantly increased in TAC/CRPtg 1 week after TAC operation compared to the other groups (Figure 6C).

Discussion

The present study demonstrated direct evidence of the pathogenic role of human CRP in pressure overload–induced cardiac remodeling, including a fall in fractional shortening and velocity of circumferential fiber shortening, promoted cardiac hypertrophy and fibrosis, and enhanced inflammation, oxidative stress, and renin-angiotensin system (RAS) activation. Interestingly, the deterioration of cardiac remodeling by CRP overexpression was preceded by an increase in macrophage infiltration, phosphorylated NF-κB/p65 in cardiomyocytes, myocardial expression of inflammatory cytokines, oxidative stress and p38 MAPK signaling, and a decrease in NO production. These findings suggest that CRP may play an important role in pressure overload–induced cardiac remodeling possibly through enhanced inflammation and oxidative stress.

Cardiac hypertrophy is considered to be an adaptive mechanism compensating for a chronic increase in pressure overload mechanical stress. However, it can become maladaptive if cardiac fibrosis develops and compensated hypertrophy evolves into cardiac failure, which is characterized by inadequate cardiac pumping activity.[13] As well as neurohormonal changes, activation of inflammatory signaling pathways by proinflammatory cytokines, such as TNF-α and IL-1β, has been considered to promote both cardiac hypertrophy and fibrosis.[14,15] Conversely, inhibition of inflammatory signaling by NF-κB ablation in TNF-α–overexpressing transgenic mice can attenuate the development of pressure overload–induced cardiac hypertrophy.[16] Xia et al[17] demonstrated upregulation of proinflammatory cytokines and leukocyte infiltration in pressure-overloaded myocardium, in association with perivascular fibrotic changes and cardiac hypertrophy, using a mouse TAC model. Although the precise mechanism causing inflammatory changes in the

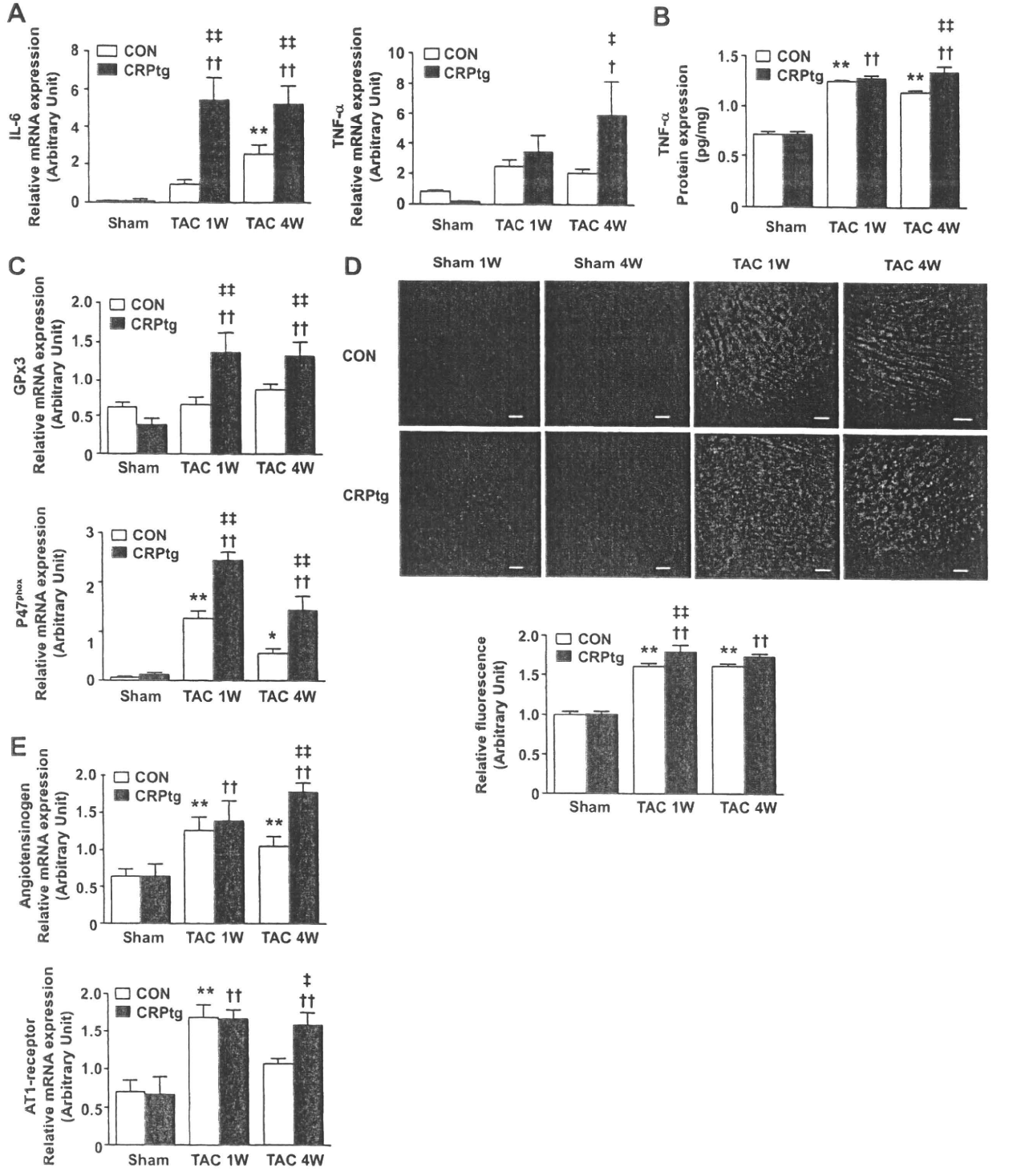

Figure 4. Inflammation, oxidative stress, and RAS. A, Expression of mRNA coding for proinflammatory cytokines (IL-6 and TNF-α). B, Protein expression of TNF-α. C, Expression of mRNA coding for oxidative stress markers (GPx3 and $P47^{phox}$). D, ROS content by DHE staining. Bars=500 μm. E, Expression of mRNA coding for RAS (angiotensinogen and AT_1R) in ventricular tissue of CRPtg and control mice 1 and 4 weeks after TAC or sham operation. *$P<0.05$, **$P<0.01$ vs Sham/CON; †$P<0.05$, ††$P<0.01$ vs Sham/CRPtg; ‡$P<0.05$, ‡‡$P<0.01$ vs TAC/CON. 1W indicates 1 week; 4W, 4 weeks.

pressure-overloaded myocardium has not been clarified, mechanical strain on the cardiomyocyte is known to induce production of IL-6, which activates the Janus kinase/signal transducer and activator of transcription (JAK/STAT) pathway and is related to myocardial hypertrophy.[18] Mechanical strain of the arterial wall is also known to induce production of ROS, proinflammatory cytokines including myocyte chemoattractant protein-1 (MCP-1), and growth factors including TGF-β1, as well as RAS activation.[19,20] MCP-1 overexpression induced by mechanical stress and RAS activation result

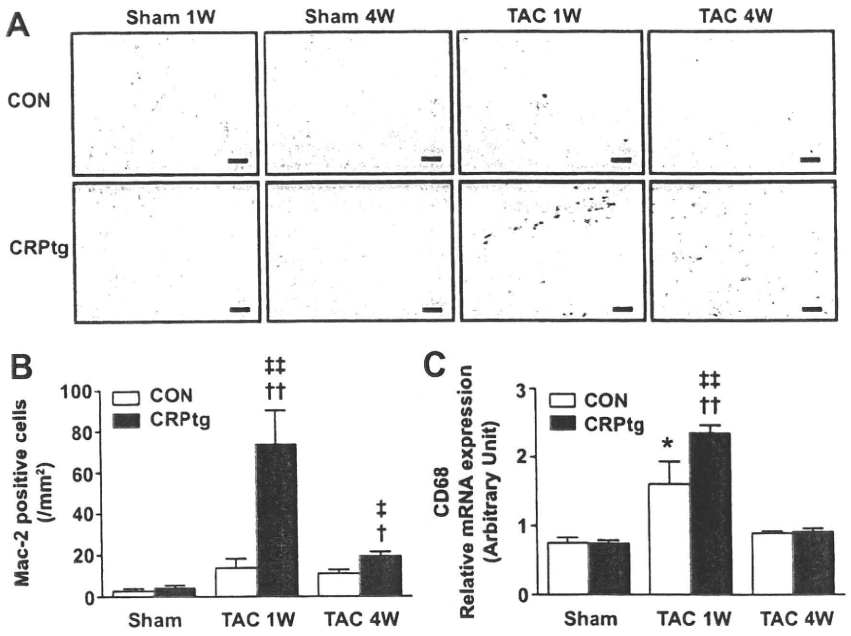

Figure 5. Infiltration of macrophages. A and B, Immunohistochemical staining for Mac-2 in left ventricle. Bar=30 μm. C, Relative expression of CD68 mRNA of CRPtg and control mice 1 and 4 weeks after TAC or sham operation. *P<0.01 vs Sham/CON; †P<0.05, ††P<0.01 vs Sham/CRPtg; ‡P<0.05, ‡‡P<0.01 vs TAC/CON. 1W indicates 1 week; 4W, 4 weeks.

in macrophage infiltration and accelerate local inflammation in a positive-feedback manner.[21] Therefore, inflammation may play a pivotal role in the process of pressure overload–induced cardiac remodeling. In fact, an inflammatory marker, serum CRP, is known to increase in heart failure patients with nonischemic etiology including hypertension and is a predictor of long-term clinical outcomes.[2]

In our results, p38 MAPK activation was enhanced in TAC/CON and further augmented in TAC/CRPtg. p38 MAPK is activated by several types of stress and inflammation and is reported to play an important role in the development of myocardial hypertrophy in a rodent chronic pressure-overloaded model.[22] Additionally, NO production was reduced in TAC/CON and further decreased in TAC/CRPtg.

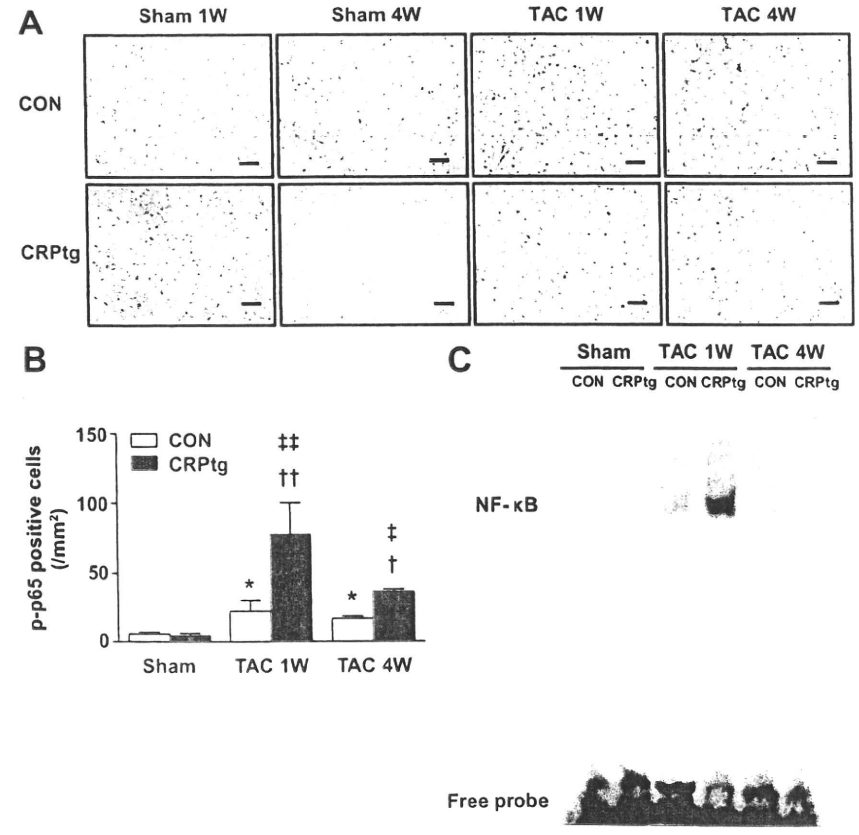

Figure 6. Activation of NF-κB/p65 in cardiomyocytes. A and B, Nuclear localization of phosphorylated NF-κB/p65 (p-p65) in cardiomyocytes of CRPtg and control mice 1 and 4 weeks after TAC or sham operation. Bar=30 μm. C, Nuclear NF-κB-DNA–binding activity by EMSA in CRPtg and control mice 1 and 4 weeks after TAC or sham operation. *P<0.05 vs Sham/CON; †P<0.05, ††P<0.01 vs Sham/CRPtg; ‡P<0.05, ‡‡P<0.01 vs TAC/CON. 1W indicates 1 week; 4W, 4 weeks.

Previous study demonstrated that NO production is impaired in the CRP overexpression mice model.[23] Therefore, our result suggests that CRP may activate p38 MAPK and impair NO production via enhancing the inflammatory response and oxidative stress.

CRP is a highly conserved acute-phase protein, secreted predominantly from the liver in response to proinflammatory cytokines, complement activation products, and hormones.[9] CRP shares many functional activities with IgG molecules, including the binding of specific ligands, opsonization of foreign molecules, and binding to FcγRs on macrophages and neutrophils. Activation of FcγR signaling results in production of proinflammatory cytokines and ROS.[24] In the setting of cardiovascular disease, elevated serum CRP is known to be associated with acceleration of atherosclerosis,[25] increased thrombosis,[26] exaggerated neointima formation after vascular injury,[27] and mural thrombosis,[28] cardiac rupture, and adverse LV remodeling[29] after myocardial infarction. Thus, CRP plays an active role originally in protecting the host from infection and injury; however, it may be related to the pathogenesis of cardiovascular complications after endogenous vascular and myocardial injury.

In the present study, overexpression of human CRP exacerbated pressure overload–induced cardiac remodeling in association with increased expression of proinflammatory cytokines, oxidative stress, p38 MAPK signaling, RAS activation, and impaired NO production. These factors synergistically activate each other and form a vicious circle during the process of cardiac remodeling. CRP overexpression might exert its effect by amplifying this vicious circle through activating each key component. The current data revealed a significant increase in the number of macrophages, NF-κB/p65–expressing myocardial cells, nuclear NF-κB-DNA–binding activity, and proinflammatory cytokine expression in the LV of CRPtg preceding the development of cardiac dysfunction after TAC operation. CRP is known to activate monocytes, macrophages, neutrophils, and endothelial cells by binding to their IgG FcγRs.[10,27,30] Moreover, CRP is capable of enhancing production of proinflammatory cytokines, including IL-6 and TNF-α, in cultured monocytes via an NF-κB–dependent mechanism.[31] These findings suggest that the effects of CRP may be mediated through activation of immunocompetent cells infiltrating into the pressure-overloaded myocardium. It could explain our observation that, in sham-operated mice in which inflammatory cell infiltration was almost absent, CRP overexpression did not show any adverse effect on cardiac function. A previous study showed that CRP itself increased fibrotic and inflammatory markers in mice fibroblasts in vitro.[8] However, the major source of proinflammatory markers in vivo is inflammatory cells, which infiltrated into the pressure-overloaded myocardium prior to the development of cardiac fibrosis. Therefore, increased expression of fibrotic and inflammatory markers in cardiac fibroblasts might contribute less to the development of pressure overload–induced cardiac remodeling.

CRP also promoted the expression of a profibrotic factor, TGF-β1, which was increased in response to pressure overload. Increased TGF-β1 may trigger the TGF-β/Smad pathway, activate fibroblasts,[8] and contribute to the promotion of cardiac fibrosis. Since the combination of hypertrophy and fibrosis causes a progressive decline in both systolic and diastolic function, increased CRP expression could be one of the determinants leading to decompensated heart failure in pressure overload.

To examine the relationship between accelerated remodeling and overexpression of human CRP, we performed anti-inflammatory therapy using eicosapentaenoic acid (EPA), which might prevent the development and progression of heart failure, especially in pressure overload–induced cardiac remodeling.[32] A recent clinical study, the GISSI-HF (Gruppo Italiano per lo Studio della Sopravvivenza nell'Infarto Miocardico-heart failure) trial, showed that a low dose of EPA administered to heart failure patients significantly decreased mortality compared to placebo.[33] One of the possible mechanisms by which EPA could prevent the development and progression of heart failure is its strong anti-inflammatory activity.[32] We treated mice with 7% EPA for 2 weeks before TAC operation and then 1 or 4 weeks after operation. Treatment with 7% EPA for 4 weeks after TAC operation resulted in reduced heart and lung weights, increased LV fractional shortening, and decreased LV end diastolic pressure, cross-sectional area, and extent of cardiac fibrosis compared to TAC/CRPtg without EPA treatment. These changes were preceded by decreased IL-6 and TNF-α mRNA expression, Mac-2–positive cell infiltration, p-p65–positive cardiomyocyte count, and oxidative stress (GPx3 and $p47^{phox}$ mRNA expression) 1 week after TAC operation (data not shown). These results suggest that EPA may suppress the adverse effects of CRP overexpression on pressure overload–induced cardiac remodeling, possibly through attenuation of the enhanced inflammatory response and oxidative stress. These findings also support the importance of an inflammation-mediated mechanism in the process of pressure overload–induced cardiac remodeling.

Perspectives

Our results showed CRP may play a pathogenic role in the progression of cardiac remodeling, thus CRP could be a candidate for a therapeutic target. Direct inhibition of CRP may reduce or eliminate the progressive inflammation, fibrosis, and hypertrophy during pressure overload-induced cardiac remodeling. This therapeutic strategy could be effective in patients with hypertension and aortic valve stenosis associated with an increased serum CRP level.

In conclusion, continuous overexpression of human CRP in mice adversely affect pressure overload-induced cardiac remodeling preceded by enhanced inflammation and oxidative stress.

CRP plays a pathogenic role in cardiac remodeling and could be a therapeutic target for the treatment of heart failure induced by pressure overload.

Acknowledgments

We thank Hiromi Kato (Keio University) and Mayu Matsuda (Keio University) for excellent technical assistance.

Sources of Funding

This work was supported by the Japanese Ministry of Education, Culture, Sports, Science, and Technology (20590872 to T.A.) and by

a Medical School Faculty and Alumni Grant from Keio University Medical Science Fund (T.A.).

Disclosures

None.

References

1. Anand IS, Latini R, Florea VG, Kuskowski MA, Rector T, Masson S, Signorini S, Mocarelli P, Hester A, Glazer R, Cohn JN. C-reactive protein in heart failure: prognostic value and the effect of valsartan. *Circulation.* 2005;112:1428–1434.
2. Kardys I, Knetsch AM, Bleumink GS, Deckers JW, Hofman A, Stricker BH, Witteman JC. C-reactive protein and risk of heart failure. The Rotterdam study. *Am Heart J.* 2006;152:514–520.
3. Araujo JP, Lourenco P, Azevedo A, Frioes F, Rocha-Goncalves F, Ferreira A, Bettencourt P. Prognostic value of high-sensitivity C-reactive protein in heart failure: a systematic review. *J Cardiol Fail.* 2009;15: 256–266.
4. Wang CH, Li SH, Weisel RD, Fedak PW, Dumont AS, Szmitko P, Li RK, Mickle DA, Verma S. C-reactive protein upregulates angiotensin type 1 receptors in vascular smooth muscle. *Circulation.* 2003;107:1783–1790.
5. Singh U, Devaraj S, Jialal I. C-reactive protein decreases tissue plasminogen activator activity in human aortic endothelial cells: evidence that C-reactive protein is a procoagulant. *Arterioscler Thromb Vasc Biol.* 2005;25:2216–2221.
6. Verma S, Wang CH, Li SH, Dumont AS, Fedak PW, Badiwala MV, Dhillon B, Weisel RD, Li RK, Mickle DA, Stewart DJ. A self-fulfilling prophecy: C-reactive protein attenuates nitric oxide production and inhibits angiogenesis. *Circulation.* 2002;106:913–919.
7. Zimmermann O, Bienek-Ziolkowski M, Wolf B, Vetter M, Baur R, Mailander V, Hombach V, Torzewski J. Myocardial inflammation and non-ischaemic heart failure: Is there a role for C-reactive protein? *Basic Res Cardiol.* 2009;104:591–599.
8. Zhang R, Zhang YY, Huang XR, Wu Y, Chung AC, Wu EX, Szalai AJ, Wong BC, Lau CP, Lan HY. C-reactive protein promotes cardiac fibrosis and inflammation in angiotensin II-induced hypertensive cardiac disease. *Hypertension.* 2010;55:953–960.
9. Szalai AJ, McCrory MA. Varied biologic functions of C-reactive protein: lessons learned from transgenic mice. *Immunol Res.* 2002;26:279–287.
10. Stein MP, Mold C, Du Clos TW. C-reactive protein binding to murine leukocytes requires Fc gamma receptors. *J Immunol.* 2000;164: 1514–1520.
11. Takahashi T, Anzai T, Kaneko H, Mano Y, Anzai A, Nagai T, Kohno T, Maekawa Y, Yoshikawa T, Fukuda K, Ogawa S. Increased C-reactive protein expression exacerbates left ventricular dysfunction and remodeling after myocardial infarction. *Am J Physiol Heart Circ Physiol.* 2010;299:H1795–H1804.
12. Rockman HA, Ross RS, Harris AN, Knowlton KU, Steinhelper ME, Field LJ, Ross J Jr, Chien KR. Segregation of atrial-specific and inducible expression of an atrial natriuretic factor transgene in an in vivo murine model of cardiac hypertrophy. *Proc Natl Acad Sci U S A.* 1991;88: 8277–8281.
13. Frey N, Olson EN. Cardiac hypertrophy: the good, the bad, and the ugly. *Annu Rev Physiol.* 2003;65:45–79.
14. Porter KE, Turner NA, O'Regan DJ, Ball SG. Tumor necrosis factor alpha induces human atrial myofibroblast proliferation, invasion and MMP-9 secretion: inhibition by simvastatin. *Cardiovasc Res.* 2004;64: 507–515.
15. Palmer JN, Hartogensis WE, Patten M, Fortuin FD, Long CS. Interleukin-1 beta induces cardiac myocyte growth but inhibits cardiac fibroblast proliferation in culture. *J Clin Invest.* 1995;95:2555–2564.
16. Higuchi Y, Chan TO, Brown MA, Zhang J, DeGeorge BR Jr, Funakoshi H, Gibson G, McTiernan CF, Kubota T, Jones WK, Feldman AM. Cardioprotection afforded by NF-kappaB ablation is associated with activation of Akt in mice overexpressing TNF-alpha. *Am J Physiol Heart Circ Physiol.* 2006;290:H590–H598.
17. Xia Y, Lee K, Li N, Corbett D, Mendoza L, Frangogiannis NG. Characterization of the inflammatory and fibrotic response in a mouse model of cardiac pressure overload. *Histochem Cell Biol.* 2009;131:471–481.
18. Pan J, Fukuda K, Saito M, Matsuzaki J, Kodama H, Sano M, Takahashi T, Kato T, Ogawa S. Mechanical stretch activates the JAK/STAT pathway in rat cardiomyocytes. *Circ Res.* 1999;84:1127–1136.
19. Capers QT, Alexander RW, Lou P, De Leon H, Wilcox JN, Ishizaka N, Howard AB, Taylor WR. Monocyte chemoattractant protein-1 expression in aortic tissues of hypertensive rats. *Hypertension.* 1997;30:1397–1402.
20. Alexander RW. Theodore cooper memorial lecture. Hypertension and the pathogenesis of atherosclerosis. Oxidative stress and the mediation of arterial inflammatory response: a new perspective. *Hypertension.* 1995; 25:155–161.
21. Kuwahara F, Kai H, Tokuda K, Niiyama H, Tahara N, Kusaba K, Takemiya K, Jalalidin A, Koga M, Nagata T, Shibata R, Imaizumi T. Roles of intercellular adhesion molecule-1 in hypertensive cardiac remodeling. *Hypertension.* 2003;41:819–823.
22. Wang Y, Huang S, Sah VP, Ross J Jr, Brown JH, Han J, Chien KR. Cardiac muscle cell hypertrophy and apoptosis induced by distinct members of the p38 mitogen-activated protein kinase family. *J Biol Chem.* 1998;273:2161–2168.
23. Grad E, Golomb M, Mor-Yosef I, Koroukhov N, Lotan C, Edelman ER, Danenberg HD. Transgenic expression of human C-reactive protein suppresses endothelial nitric oxide synthase expression and bioactivity after vascular injury. *Am J Physiol Heart Circ Physiol.* 2007;293:H489–H495.
24. Melendez A, Floto RA, Cameron AJ, Gillooly DJ, Harnett MM, Allen JM. A molecular switch changes the signalling pathway used by the Fc gamma RI antibody receptor to mobilise calcium. *Curr Biol.* 1998;8: 210–221.
25. Paul A, Ko KW, Li L, Yechoor V, McCrory MA, Szalai AJ, Chan L. C-reactive protein accelerates the progression of atherosclerosis in apolipoprotein E-deficient mice. *Circulation.* 2004;109:647–655.
26. Danenberg HD, Szalai AJ, Swaminathan RV, Peng L, Chen Z, Seifert P, Fay WP, Simon DI, Edelman ER. Increased thrombosis after arterial injury in human C-reactive protein-transgenic mice. *Circulation.* 2003; 108:512–515.
27. Xing D, Hage FG, Chen YF, McCrory MA, Feng W, Skibinski GA, Majid-Hassan E, Oparil S, Szalai AJ. Exaggerated neointima formation in human C-reactive protein transgenic mice is IgG Fc receptor type 1 (Fc gamma RI)-dependent. *Am J Pathol.* 2008;172:22–30.
28. Anzai T, Yoshikawa T, Kaneko H, Maekawa Y, Iwanaga S, Asakura Y, Ogawa S. Association between serum C-reactive protein elevation and left ventricular thrombus formation after first anterior myocardial infarction. *Chest.* 2004;125:384–389.
29. Anzai T, Yoshikawa T, Shiraki H, Asakura Y, Akaishi M, Mitamura H, Ogawa S. C-reactive protein as a predictor of infarct expansion and cardiac rupture after a first Q-wave acute myocardial infarction. *Circulation.* 1997; 96:778–784.
30. Bharadwaj D, Stein MP, Volzer M, Mold C, Du Clos TW. The major receptor for C-reactive protein on leukocytes is Fcgamma receptor II. *J Exp Med.* 1999;190:585–590.
31. Hanriot D, Bello G, Ropars A, Seguin-Devaux C, Poitevin G, Grosjean S, Latger-Cannard V, Devaux Y, Zannad F, Regnault V, Lacolley P, Mertes PM, Hess K, Longrois D. C-reactive protein induces pro- and anti-inflammatory effects, including activation of the liver x receptor alpha, on human monocytes. *Thromb Haemost.* 2008;99:558–569.
32. Duda MK, O'Shea KM, Tintinu A, Xu W, Khairallah RJ, Barrows BR, Chess DJ, Azimzadeh AM, Harris WS, Sharov VG, Sabbah HN, Stanley WC. Fish oil, but not flaxseed oil, decreases inflammation and prevents pressure overload-induced cardiac dysfunction. *Cardiovasc Res.* 2009;81: 319–327.
33. Tavazzi L, Maggioni AP, Marchioli R, Barlera S, Franzosi MG, Latini R, Lucci D, Nicolosi GL, Porcu M, Tognoni G. Effect of n-3 polyunsaturated fatty acids in patients with chronic heart failure (the GISSI-HF trial): a randomised, double-blind, placebo-controlled trial. *Lancet.* 2008; 372:1223–1230.

Quantitative Analysis of Right Ventricular Function in Patients With Pulmonary Hypertension Using Three-Dimensional Echocardiography and a Two-Dimensional Summation Method Compared to Magnetic Resonance Imaging

Tomoko Morikawa, MD[a,†], Mitsushige Murata, MD, PhD[b,*,†], Shigeo Okuda, MD, PhD[c], Hikaru Tsuruta, MD[a], Shiro Iwanaga, MD, PhD[a], Mitsuru Murata, MD, PhD[b], Toru Satoh, MD, PhD[d], Satoshi Ogawa, MD, PhD[e], and Keiichi Fukuda, MD, PhD[a]

Magnetic resonance imaging (MRI) is considered the clinical reference standard for measuring the right ventricular (RV) volume and ejection fraction, although real-time 3-dimensional echocardiography (RT3DE) would be a preferred method owing to its convenience and availability for repetitive examinations. However, the feasibility, accuracy, and reproducibility of RT3DE have not been fully examined. The present study sought to validate the correlation of RT3DE with a 2-dimensional summation method compared to MRI for assessing the function of the right ventricle and to evaluate the RV function in patients with pulmonary hypertension (PH). Thirty patients with PH underwent both RT3DE and MRI. The right ventricle was reconstructed with RT3DE using a 2-dimensional summation method to analyze the MRI measurements. The RV end-diastolic volume, RV end-systolic volume, and RV ejection fraction were measured. Fifteen normal subjects underwent the same echocardiographic protocol for comparison. The RV end-diastolic volume index, RV end-systolic volume index, and RV ejection fraction measured using RT3DE correlated well with those measured using MRI ($R = 0.96$, $p < 0.001$; $R = 0.96$, $p < 0.001$; $p = 0.93$, and $p < 0.001$, respectively). All inter- and intraobserver variability values for the RV end-diastolic volume, RV end-systolic volume, and RV ejection fraction were <17%. Both the RV end-diastolic volume index and the RV end-systolic volume index were significantly enlarged in those with PH compared to those in the normal subjects (RVEDVI 123 ± 42 ml/m^2 vs 74 ± 12 ml/m^2; RVESVI 86 ± 33 ml/m^2 vs 26 ± 5 ml/m^2 in those with PH and the normal subjects, respectively, $p < 0.0001$). In contrast, the RV ejection fraction was significantly reduced in the patients with PH compared to that in the normal subjects (30 ± 12% vs 65 ± 6%, respectively, $p < 0.01$). Thus, RT3DE with a 2-dimensional summation method might provide comparable and feasible measurements of the RV volume in patients with PH compared to MRI. **(Am J Cardiol 2011;107:484–489)**

The present study sought to clarify the accuracy, feasibility, and reproducibility of real-time 3-dimensional echocardiography (RT3DE) with a 2-dimensional (2D) summation method for assessing the right ventricular (RV) volume and function. We compared it to the reference standard of magnetic resonance imaging (MRI) measurement. We also evaluated the RV function in patients with pulmonary hypertension (PH).

Methods

We performed a cross-sectional study that enrolled 45 subjects (14 men; mean age 51 ± 16 years). The group included 15 subjects with echocardiographically normal hearts and an estimated pulmonary artery systolic pressure <30 mm Hg using 2D echocardiography and 30 patients with pulmonary hypertension (PH). PH was defined by an estimated pulmonary artery systolic pressure >50 mm Hg, as measured using Doppler echocardiography. The patient group consisted of 7 patients with chronic pulmonary embolism and 23 with pulmonary arterial hypertension (15 patients with primary PH, 6 with autoimmune disease, and 2 with an atrial septal defect). All patients with PH underwent both RT3DE and MRI. All subjects underwent 2D echocardiography to exclude left-heart disease and to assess the presence of tricuspid insufficiency. The exclusion criteria were contraindications to MRI, the presence of arrhythmia, age <20 or >70 years, and pregnancy. The ethics committee of Keio University Hospital approved the study.

From the Departments of [a]Cardiology, [b]Laboratory Medicine, and [c]Diagnostic Radiology, Keio University School of Medicine, Tokyo, Japan; [d]Second Department of Internal Medicine, Kyorin University School of Medicine, Tokyo, Japan; and [e]International University of Health and Welfare, Mita Hospital, Tokyo, Japan. Manuscript received July 12, 2010; manuscript received and accepted September 18, 2010.

*Corresponding author: Tel: (+81) 3-5363-3874; fax (+81) 3-5363-3875.

E-mail address: muratam@sc.itc.keio.ac.jp (M. Murata).

† Tomoko Morikawa and Mitsushige Murata equally contributed to this work.

0002-9149/11/$ – see front matter
doi:10.1016/j.amjcard.2010.09.047

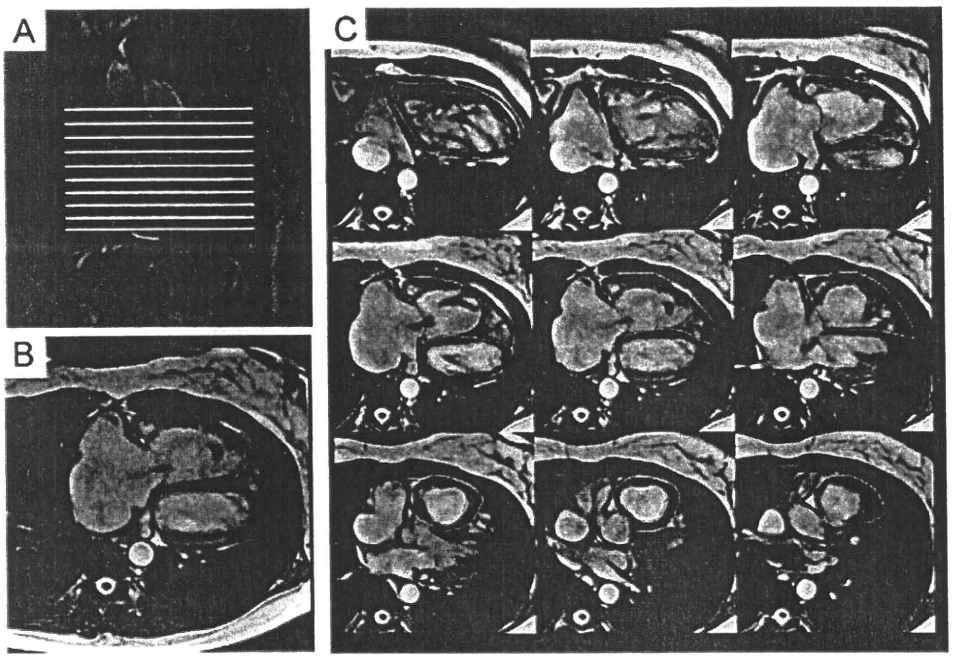

Figure 1. Data analysis by MRI. *(A,B)* A reference image was used to derive multiple parallel slices of the right ventricle. *(C)* Series of corresponding contiguous vertical slice images of right ventricle from apex to RV outflow tract, as shown in *Figure A*. Endocardial borders were manually traced at end-systole and end-diastole to calculate the RV volume and ejection fraction.

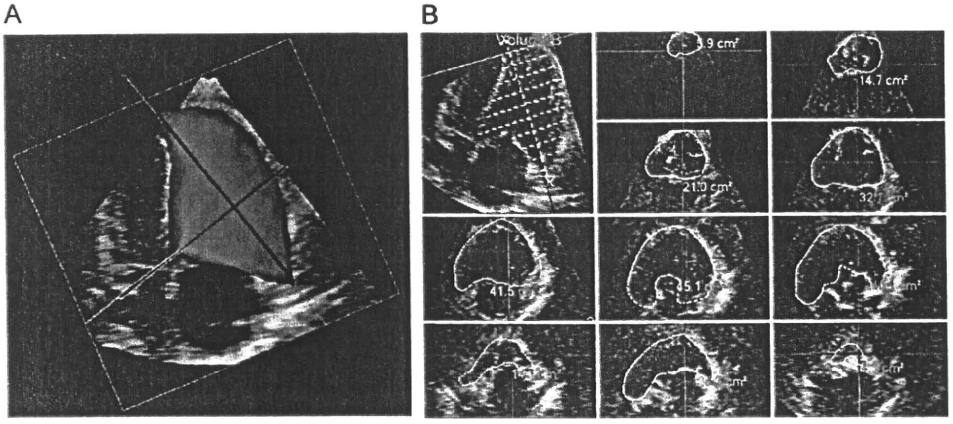

Figure 2. Off-line analysis of RT3DE data using disk summation algorithm for RV volume calculations at end-diastole. *(A)* RV reconstruction. *(B)* Four-chamber view and series of contiguous short-axis slices of right ventricle. Endocardial borders were traced manually at end-diastole and end-systole to calculate the RV volume and ejection fraction.

Cardiac MRI scans were obtained using a 1.5-Tesla clinical scanner (GE Healthcare, Milwaukee, Wisconsin). For the RV volume measurements, contiguous transverse images were acquired through the entire right ventricle using a 2D cine, steady-state, free precession technique with prospective electrocardiographic gating (Figure 1). Each cross-section image was obtained in a single breath hold with the following parameters: repetition time 3.2 ms, echo time 1.6 ms, flip angle 45°, bandwidth 125 kHz, field of view 350 × 350 mm^2, matrix size 224 × 192, slice thickness 10 mm without a gap, and 20 phases during one cardiac cycle. The in-plane resolution was 1.6 × 1.8 mm^2. The cardiac MRI examination time was approximately 30 minutes and included short-axis images of the left ventricle to evaluate the left ventricular function, after transverse images of the right ventricle. Post processing was performed on a workstation (AdvantageWorkstation, GE Healthcare, Milwaukee, Wisconsin). The endocardial borders of all images at end-diastole and end-systole were manually traced by a radiologist with 10 years' experience of cardiac MRI. The end-diastolic volume, end-systolic volume, and ejection fraction were automatically calculated using Simpson's rule. The inclusion of the trabeculae carneae in the RV volume was the same as that used in the ultrasound methods for comparison. Fewer than 15 minutes were required for RV volume measurement.

Figure 2 shows the 3D RV reconstruction using the RT3DE analysis. Using iE33 (Philips Medical Systems, Bothell, Washington), the RT3D echocardiographic images were obtained from the apical window with the patient in the same position as for 2D echocardiography.

Table 1
Clinical characteristics

Variable	Normal (n = 15)	Patients With PH (n = 30)
Age (years)	56 ± 19	50 ± 15
Women (n)	8 (53%)	21 (70%)
Height (cm)	161 ± 7	158 ± 9
Body weight (kg)	55 ± 9	55 ± 13
Body surface area (m^2)	1.6 ± 0.2	1.5 ± 0.2
Left ventricular end-diastolic diameter (mm)	43 ± 3	39 ± 8
Left ventricular end-systolic diameter (mm)	26 ± 3	23 ± 6
Left ventricular ejection fraction (%)	78 ± 5	77 ± 13
Pulmonary artery systolic pressure (mm Hg)	27 ± 5	99 ± 22*

No significant difference was found in left ventricular function between the 2 groups; however, pulmonary artery systolic pressure was significantly increased in the PH group compared with that in the normal subjects.
* $p < 0.05$ vs normal.

The images were also gathered for 5 cardiac cycles using a matrix array transducer. The acquisition time for RT3DE was 1 to 2 minutes. Off-line analyses were blindly performed by 2 independent observers using a General Imaging 3DQ Plug-in with the Advanced Q-Laboratory analysis software (Philips Medical Systems). The long axis from the apex to the area around the tricuspid valve was determined, and 10 cross-sections were observed at an even distance apart. The ellipse was manually traced to the endocardial borders of each cross section, just as for the MRI procedure. All the ellipses were then stacked to reconstruct the whole intracardial space of the right ventricle in 3 dimensions. The 3D representation of the right ventricle was observed from different directions and then revised with respect to the inappropriate traces to complete the analysis. The measurement time for RT3DE was approximately 10 to 30 minutes.

The pressure gradient of tricuspid regurgitation was measured using continuous wave Doppler imaging. The mean right atrial pressure was estimated from the diameter and collapsibility of the inferior vena cava, as reported previously.[1,2] Next, the pulmonary arterial systolic pressure was calculated by summation of the pressure gradient of the tricuspid regurgitation and right atrial pressure.

The results for the RV end-diastolic volume, end-systolic volume, and ejection fraction are presented as the mean ± SD. Correlations were determined between the echocardiographic and MRI measurements, and agreement was expressed according to the Bland-Altman method. p Values <0.05 were considered statistically significant. The statistical analysis was performed using the Statistical Package for Social Sciences, version 10 (SPSS, Chicago, Illinois).

Results

Table 1 lists the clinical characteristics for the normal subjects and patients with PH. We first validated the measurement for RV function using RT3DE compared with that obtained using MRI analysis. Visualization of the RV free wall, tricuspid valve, RV outflow tract, and apex were feasible with both RT3DE and MRI, although poor endocardial definition in at least one view precluded a quantitative assessment. The RV parameters measured by both RT3DE and MRI included the RV end-diastolic volume, RV end-diastolic volume indexed to the body surface area (RV end-diastolic volume index), RV end-systolic volume, RV end-systolic volume indexed to body surface area (RV end-systolic volume index), RV ejection fraction, and pulmonary artery systolic pressure. The RV parameters measured with RT3DE by the 2 observers were averaged for comparison with those obtained with MRI. The 2 sets of values were close for all parameters (Table 2), and Figure 3 demonstrates the strong correlation between RT3DE and MRI measurements for the RV end-diastolic volume index, RV end-systolic volume index, and RV ejection fraction.

Table 2
Parameters measured with real-time three-dimensional echocardiography (RT3DE) and magnetic resonance imaging (MRI) in patients with pulmonary hypertension (PH)

Parameter	RT3DE (n = 30)	MRI (n = 30)
Right ventricular end-diastolic volume (ml)	203 ± 60	202 ± 63
Right ventricular end-systolic volume (ml)	139 ± 53	137 ± 57
Right ventricular end-diastolic volume index (ml/m^2)	203 ± 60	202 ± 63
Right ventricular end-systolic volume index (ml/m^2)	92 ± 36	90 ± 38
Right ventricular ejection fraction (%)	32 ± 13	33 ± 14

A Bland-Altman plot showed small mean differences and limits of agreement in the measurements of the RV end-diastolic volume index, RV end-systolic volume index, and RV ejection fraction between RT3DE and MRI (−9.0 ± 12 ml/m^2, −3.5 ± 9.6 ml/m^2, and −3.1 ± 5.4%, respectively; Figure 4).

Two independent observers performed the same analyses. A good correlation in the RV end-diastolic volume index measurements was obtained between them (Figure 5). The Bland-Altman plot of the differences by the 2 observers showed a significant mean difference and limits of agreement (Figure 5). The interobserver variability was −19 ± 42 ml/m^2, 6 ± 16 ml/m^2, and −1 ± 10% for the RV end-diastolic volume, RV end-systolic volume, and RV ejection fraction, respectively.

The intraobserver variability was also assessed. Two analyses of the RV end-diastolic volume index measurements by the same observer correlated strongly (Figure 5), and the Bland-Altman plot of the differences by the same observer showed low mean differences and limits of agreement (Figure 5). The intraobserver variability was −0.4 ± 4.0 ml/m^2, −0.5 ± 12 ml/m^2, and 0.6 ± 9% for the RV end-diastolic volume, RV end-systolic volume, and RV ejection fraction, respectively.

The RV function differed somewhat between those with PH and the normal subjects (Figure 6). Both the RV end-diastolic volume index and RV end-systolic volume index were significantly enlarged, and the RV ejection fraction

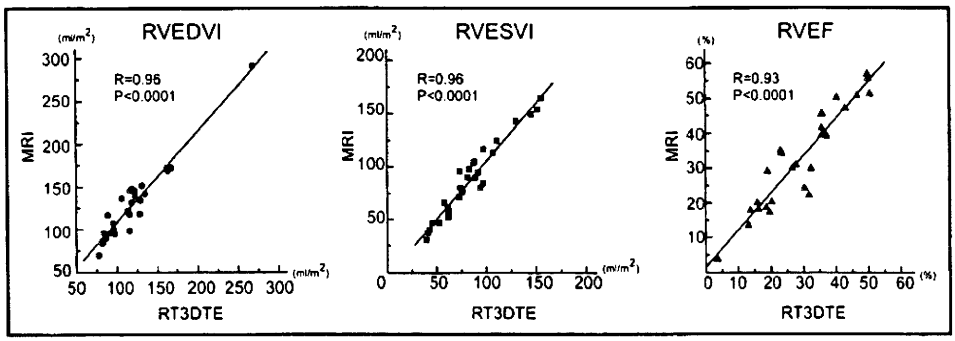

Figure 3. Comparisons between RT3DE and MRI measurements of RV volume and ejection fraction. These plots show the linear regression analysis of RT3DE-derived RV end-diastolic volume index (RVEDVI), RV end-systolic volume index (RVESVI), and RV ejection fraction (RVEF) against MRI reference values obtained for 30 patients with PH. RVEDVI, RVESVI, and RVEF correlated strongly between RT3DE and MRI analyses.

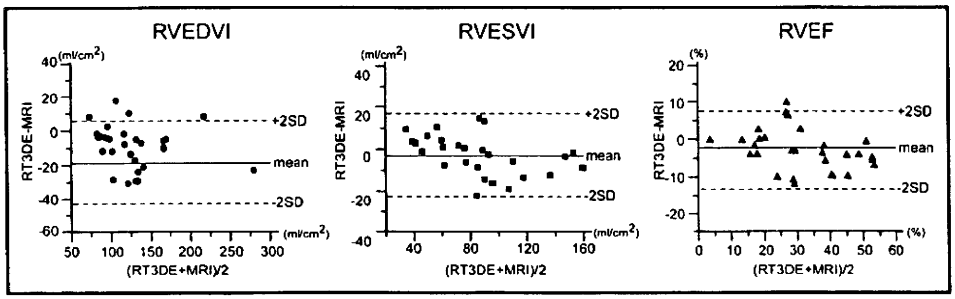

Figure 4. Bland-Altman analyses between RT3DE and MRI measurements of RV volume and ejection fraction. *Solid lines* on Bland-Altman plots indicate mean differences; *dashed line* indicates limits of agreement.

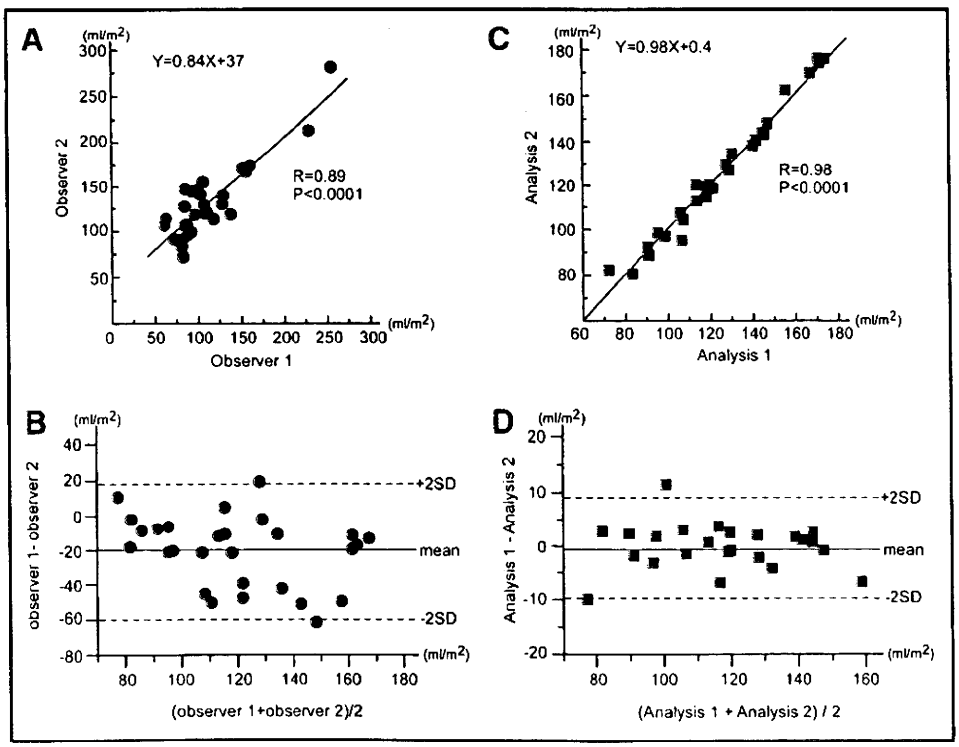

Figure 5. Interobserver and intraobserver variances for measurement of RV end-diastolic volume index (RVEDVI) by RT3DE. *(A)* Linear regression of RVEDVI measured by 2 independent observers. *(B)* Bland-Altman analysis for RVEDVI between 2 independent observers. *(C)* Linear regression analysis of RVEDVI measurements by same observer. *(D)* Bland-Altman analysis for RVEDVI between 2 independent analyses by the same observer.

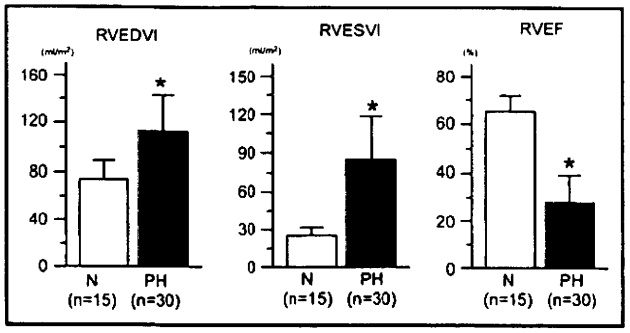

Figure 6. RV volumes and ejection fractions in patients with PH. Comparison of RV end-diastolic volume index (RVEDVI), RV end-systolic volume index (RVESVI), and RV ejection fraction (RVEF) between normal subjects (N, n = 15) and PH (n = 30). *p <0.01 versus normal subjects; error bars indicate SD.

was reduced in the patients with PH compared to that of the normal subjects.

Discussion

The assessment of RV function using conventional 2D echocardiography remains difficult owing to the inherently complicated geometry.[3–5] The results of the present study have demonstrated that measuring the RV volume and function using RT3DE with a 2D summation method was feasible and reliable compared to MRI, validating the method as an alternative technique in cardiac functional assessment. A previous study provided some validation of the RV measurement by RT3DE using a 3D volume acquisition method against MRI.[6] However, the present identical analysis using a 2D summation method would be the preferred comparison because of its closer similarity with the MRI analysis and consequent reduction in error owing to different algorithms being applied to derive the RV reconstruction. In the present study, the values of each RV parameter measured with our method were very close to those determined using MRI, specifically the RV end-diastolic volume index, RV end-systolic volume index, and RV ejection fraction. In addition, we used a General Imaging 3DQ Plug-in with the Advanced Q-Laboratory analysis software equipped with a Philips iE33 ultrasound machine for the 2D summation method. Although cardiac 3DQ plug-ins are generally used for left ventricular analysis, it was not deemed suitable for RV analysis because of its auto-trace function. Considering the complex shape and structure of variable intracardiac space in the right ventricle, auto-tracing could be difficult to adopt for these atypical shapes, resulting in inaccurate tracings as input for the analysis. After prudent discussions with a radiologist experienced in analyzing cardiac MRI before the present study, we used manual tracing for the 2D summation method, using sample images of the right ventricle from cardiac MRI and RT3DE. We ensured that the intracardiac-border end points were identical for both MRI and RT3DE, including the trabeculae carneae. In both methods, 9 to 10 cross-sections were traced in all subjects, while maintaining the blind analysis.

Cardiac MRI enables the structure of the right ventricle to be visualized for measurements of the RV volume and systolic function. However, problems such as the expense and duration of the procedure and the limited availability to patients with implanted devices did not allow us to monitor the RV function analysis using repetitive MRI examination. In addition, cardiac MRI requires a lengthy breath-hold for the necessary acquisition of scanning, which could be painful for patients with heart failure. In contrast, echocardiography is convenient, inexpensive, and tolerant for repetitive examination even in patients with implantable devices. Some patients with severe PH have intravenous infusion pump devices fitted for continuous administration of medication,[7–9] possibly rendering them ineligible for MRI. In these cases, RT3DE would provide an ideal alternative for evaluating the RV volume and function.

The pulmonary artery systolic pressure is the hemodynamic parameter taken to reflect the clinical severity of PH.[10] However, our data revealed a significant, but very weak, correlation between the pulmonary artery systolic pressure and the RV ejection fraction, suggesting that the pulmonary artery systolic pressure does not reflect RV systolic dysfunction. Therefore, a symptomatic patient might need to undergo RT3DE and careful evaluation of the RV function even after their pulmonary artery systolic pressure has been attenuated by medical therapy.

The differences in spatial resolution between RT3DE and MRI might affect the comparison to a variable degree. In MRI examinations, a contrast drug can enhance the border between the intracardiac cavity and endocardium, thus maintaining the spatial resolution. In contrast, the endocardial definition is sometimes difficult to discern in the right ventricle by RT3DE owing to artifacts and the abundant aberrant papillary muscles in the right ventricle. This might cause a significant mean difference in the measurements of the RV end-diastolic volume index between RT3DE and MRI. However, this difference was small in the present study, and RT3DE might therefore be sufficient to evaluate the global RV systolic function.

RT3DE also has a limitation with respect to data acquisition in patients with arrhythmias, including atrial fibrillation and frequent extrasystoles, because acquisition of 5 consecutive, stable heart beats is necessary for 3D image reconstruction. Future technological development in data acquisition with RT3DE is needed to overcome this limitation.

Acknowledgment: We thank Dr. Keisuke Kouyama and Takayuki Abe for statistical analysis, and Ms. Makiko Dan, Kumiko Tomiyama, Yasuko Hatori, Akemi Okamoto, Makiko Kondo, and Junko Shinohara for technical assistance.

1. Moreno FL, Hagan AD, Holmen JR, Pryor TA, Strickland RD, Castle CH. Evaluation of size and dynamics of the inferior vena cava as an index of right-sided cardiac function. *Am J Cardiol* 1984;53:579–585.
2. Simonson JS, Sonospirometry SNB. A new method for noninvasive estimation of mean right atrial pressure based on two-dimensional echographic measurements of the inferior vena cava during measured inspiration. *J Am Coll Cardiol* 1988;11:557–564.

3. Jauhiainen T, Jarvinen VM, Hekali PE, Poutanen VP, Penttila A, Kupari M. Gradient echo volumetric analysis of human cardiac casts: focus on the right ventricle. *J Comput Assist Tomogr* 1998;22:899–903.
4. Mogelvang J, Stubgaard M, Thomsen C, Henriksen O. Evaluation of right ventricular volumes measured by magnetic resonance imaging. *Eur Heart J* 1988;9:529–533.
5. Dekker DL, Piziali RL, Dong E Jr. A system for ultrasonically imaging the human heart in three dimensions. *Comput Biomed Resour* 1974; 7:544–553.
6. Niemann PS, Pinho L, Balbach T, Galuschky C, Blankenhagen M, Silberbach M, Broberg C, Jerosch-Herold M, Sahn DJ. Anatomically oriented right ventricular volume measurements with dynamic three-dimensional echocardiography validated by 3-Tesla magnetic resonance imaging. *J Am Coll Cardiol* 2007;50:1668–1676.
7. McLaughlin VV, Genthner DE, Panella MM, Rich S. Reduction in pulmonary vascular resistance with long-term epoprostenol (prostacyclin) therapy in primary pulmonary hypertension. *N Engl J Med* 1998;338:273–277.
8. Rubin LJ. Primary pulmonary hypertension. *N Engl J Med* 1997;336: 111–117.
9. Rubin LJ, Badesch DB. Evaluation and management of the patient with pulmonary arterial hypertension. *Ann Intern Med* 2005;143:282–292.
10. Schannwell CM, Steiner S, Strauer BE. Diagnostics in pulmonary hypertension. *J Physiol Pharmacol* 2007;58(Suppl 5):591–602.

Cell Metabolism

Crosstalk between Glucocorticoid Receptor and Nutritional Sensor mTOR in Skeletal Muscle

Noriaki Shimizu,[1,10] Noritada Yoshikawa,[1,2,10] Naoki Ito,[3,4] Takako Maruyama,[1] Yuko Suzuki,[3] Sin-ichi Takeda,[3] Jun Nakae,[5] Yusuke Tagata,[9] Shinobu Nishitani,[9] Kenji Takehana,[9] Motoaki Sano,[6] Keiichi Fukuda,[6] Makoto Suematsu,[7,8] Chikao Morimoto,[1,2] and Hirotoshi Tanaka[1,2,*]

[1]Division of Clinical Immunology, Advanced Clinical Research Center
[2]Department of Rheumatology and Allergy, Research Hospital
Institute of Medical Science, University of Tokyo, Tokyo 108-8639, Japan
[3]Department of Molecular Therapy, National Institute of Neuroscience, National Center of Neurology and Psychiatry, Kodaira 187-8502, Japan
[4]Department of Biological Information, Tokyo Institute of Technology, Yokohama 226-8501, Japan
[5]Frontier Medicine on Metabolic Syndrome, Division of Endocrinology, Metabolism and Nephrology, Department of Internal Medicine
[6]Cardiology Division, Department of Internal Medicine
[7]Department of Biochemistry
[8]JST ERATO, Suematsu Gas Biology Project
Keio University School of Medicine, Tokyo 160-8582, Japan
[9]Ajinomoto Pharmaceuticals Co., Ltd., Kawasaki 210-8681, Japan
[10]These authors contributed equally to this work
*Correspondence: hirotnk@ims.u-tokyo.ac.jp
DOI 10.1016/j.cmet.2011.01.001

SUMMARY

Maintenance of skeletal muscle mass relies on the dynamic balance between anabolic and catabolic processes and is important for motility, systemic energy homeostasis, and viability. We identified direct target genes of the glucocorticoid receptor (GR) in skeletal muscle, i.e., REDD1 and KLF15. As well as REDD1, KLF15 inhibits mTOR activity, but via a distinct mechanism involving BCAT2 gene activation. Moreover, KLF15 upregulates the expression of the E3 ubiquitin ligases atrogin-1 and MuRF1 genes and negatively modulates myofiber size. Thus, GR is a liaison involving a variety of downstream molecular cascades toward muscle atrophy. Notably, mTOR activation inhibits GR transcription function and efficiently counteracts the catabolic processes provoked by glucocorticoids. This mutually exclusive crosstalk between GR and mTOR, a highly coordinated interaction between the catabolic hormone signal and the anabolic machinery, may be a rational mechanism for fine-tuning of muscle volume and a potential therapeutic target for muscle wasting.

INTRODUCTION

Muscle comprises ~40% of body mass and contributes not only to the structure and movement of the body but also to nutrient storage and supply (Matthews, 1999). In adult mammals, skeletal muscle hypertrophy/atrophy is characterized by an increase/decrease in the size (as opposed to the number) of individual myofibers, respectively. The control of muscle mass is believed to be determined by a dynamic balance between anabolic and catabolic processes (Hoffman and Nader, 2004). Mammalian target of rapamycin (mTOR) is a crucial component of the anabolic machinery for protein synthesis. mTOR consists of two complexes: mTORC1, which includes Raptor, signals to S6K and 4E-BP1, controls protein synthesis, and is rapamycin sensitive; and mTORC2, which includes Rictor, signals to Akt, and is rapamycin insensitive. mTORC1 integrates four major signals: growth factors, energy status, oxygen, and amino acids, especially branched-chain amino acids (BCAAs). Prototypically, insulin/IGF-1 activates mTOR via the PI3K-Akt pathway (Sengupta et al., 2010). It is currently considered that mTORC1, and not mTORC2, is essential for the maintenance of muscle mass and function (Bentzinger et al., 2008; Risson et al., 2009). Protein degradation in skeletal muscle cells is essentially mediated by the activity of two conserved pathways: the ubiquitin-proteasomal pathway and the autophagic/lysosomal pathway (Sandri, 2008). The ubiquitin-proteasomal pathway is responsible for the turnover of the majority of soluble and myofibrillar muscle proteins. The activity of this pathway is markedly increased in atrophying muscle due to the transcriptional activation of a set of E3 ligase-encoding genes, e.g., atrogin-1 and MuRF1 (Glass, 2003; Sandri et al., 2004). Autophagy also plays an important role in the degradation of skeletal muscle, and is indicated to be a consequence of an ordered transcriptional program involving a battery of genes, e.g., LC3 and Bnip3 (Mizushima et al., 2008). These positive and negative pathways are balanced in a highly coordinated manner for the determination of myofiber size and total muscle volume; however, distortion of this balance with a relative increase in degradation results in the generalized decrease of myofiber size and muscle atrophy (Hoffman and Nader, 2004). Pioneering studies demonstrated that muscle atrophy is a result of active processes that are transcriptionally controlled through the expression of a particular gene set; the forkhead box O (FoxO) transcription factors are

common components of a number of atrophy models and act as critical liaison molecules for protein degradation and autophagy via the transcriptional regulation of, for example, atrogin-1, MuRF1, LC3, and Bnip3 (Mammucari et al., 2007; Sandri et al., 2004; Stitt et al., 2004; Zhao et al., 2007). In clear contrast, it is evident that each disease has proper signaling pathways to FoxOs and that other components of the cellular machinery often participate in the progression of atrophy (Moresi et al., 2010; Suzuki et al., 2007). Therefore, for the development of therapies against muscle atrophy, it should be addressed how the transcriptional program triggered by a particular atrophy pathway is orchestrated and how the balance of muscle protein synthesis and degradation is distorted in each disease.

Adrenal glucocorticoids produce their actions via a signal pathway involving the ubiquitously expressed glucocorticoid receptor (GR), a prototypic member of the nuclear receptor superfamily, which acts as a ligand-dependent transcription factor. Upon binding glucocorticoids, GR translocates into the nucleus and binds to the glucocorticoid response element (GRE) in the promoters of target genes. The binding of liganded receptors to target DNA is followed by the recruitment of mediators and coactivators to the proximity of GRE, resulting in the recruitment of RNA polymerase II (RNAPII) to nearby transcription start sites and the activation of transcription (Evans, 2005; Meijsing et al., 2009). In skeletal muscle, glucocorticoids elicit a variety of biological actions in the metabolism of glucose, lipids, and proteins and contribute to metabolic homeostasis (Munck et al., 1984). On the other hand, the prolonged oversecretion or exogenous administration of glucocorticoid gives rise to undesirable effects including muscle atrophy (Munck et al., 1984). Although many studies addressed the mechanism of glucocorticoid-induced muscle atrophy, how the glucocorticoid-GR system generates the functional coupling between metabolic regulation and volume adjustment in skeletal muscle remains unsolved. Of note, many pathological conditions characterized by muscle atrophy, e.g., sepsis, cachexia, starvation, metabolic acidosis, and severe insulinopenia, are associated with an increase in circulating glucocorticoid levels. Adrenalectomy or treatment with the GR antagonist RU486 attenuates muscle atrophy in sepsis, cachexia, starvation, and severe insulinopenia (Menconi et al., 2007; Schakman et al., 2008). Moreover, endogenous glucocorticoids were shown to be essential for muscle atrophy in acute diabetic rodents (Hu et al., 2009). Together, understanding the glucocorticoid-mediated regulation of metabolism-volume coupling in muscle is increasingly important for the management of not only muscle atrophy but also these wasting/metabolic disorders.

Typically, glucocorticoid-induced muscle atrophy is characterized by fast-twitch type II glycolytic muscle fiber loss with reduced or no impact on type I fibers. The mechanism of such fiber specificity is yet unknown. Previous reports suggested that the glucocorticoid-GR system has antianabolic and catabolic effects and promotes degradation via the induction of a set of genes including atrogin-1, MuRF1, and myostatin (Menconi et al., 2007; Schakman et al., 2008). Although the involvement of FoxO transcription factors is reported in the gene regulation of atrogin-1 and MuRF1 under the presence of excess glucocorticoids (Sandri et al., 2004; Stitt et al., 2004), the biochemical role of GR in the transcriptional regulation of muscle tissue has not yet been determined. Therefore, we investigated how GR-mediated gene expression coordinately modulates antianabolic and catabolic actions to understand the functional coupling of metabolism and volume regulation in muscle.

In the present study, we identified REDD1 and KLF15 genes as direct targets of GR. REDD1 is known to be induced by various stressors, including glucocorticoid, and to inhibit mTOR activity via the sequestration of 14-3-3 and the increase of TSC1/2 activity (Wang et al., 2006; DeYoung et al., 2008). We clearly identified the functional GRE via the promoter analysis of REDD1 gene. On the other hand, KLF15 is a recently discovered transcription factor that is involved in several metabolic processes in skeletal muscle; e.g., KLF15 transcriptionally upregulates the gene expression of branched-chain aminotransferase 2 (BCAT2), a mitochondrial enzyme catalyzing the first reaction in the catabolism of BCAA to accelerate BCAA degradation and alanine production in skeletal muscle (Gray et al., 2007). Moreover, phenotypic analysis of cardiac-specific KLF15 knockout mice revealed marked left ventricular hypertrophy, indicating the negative regulatory role of KLF15 on muscle mass (Fisch et al., 2007). We here demonstrated that KLF15 participates in muscle catabolism via the transcriptional regulation of atrogin-1 and MuRF1. Moreover, KLF15 affects mTOR through BCAA degradation and negatively modulates myofiber size. mTOR activation inhibits GR-mediated transcription by suppressing GR recruitment onto target genes, strongly suggesting a mutually exclusive crosstalk between mTOR and GR. Pharmacological activation of mTOR with BCAA attenuated GR-mediated gene expression, leading to the substantial restoration of muscle in glucocorticoid-treated rats. We, therefore, indicate the critical importance of the interaction of GR and mTOR in the regulation of metabolism-volume coupling in skeletal muscle.

RESULTS

REDD1 and KLF15 Are Target Genes of GR in Skeletal Muscle

GR levels were relatively high in type II-rich gastrocnemius and tibialis anterior muscles compared to type I-rich soleus muscle in rats (Figure 1A). Figure 1B illustrates the comparison of the effects of a 3 hr treatment with dexamethasone (DEX) on mRNA expression of various genes between the gastrocnemius and soleus muscles. Hormonal induction of mRNA expression of REDD1, atrogin-1, MuRF1, KLF15, FoxO1, FoxO3, and myostatin, as well as the well-known GR target gene FKBP5 (Yoshikawa et al., 2009), was observed in both muscles, but to a lesser extent in the soleus muscle. Among the genes induced by DEX at 3 hr (Figure 1B), the promoter regions of MuRF1 (Waddell et al., 2008) and myostatin (Ma et al., 2001), but not atrogin-1 (Sandri et al., 2004), contain functional GREs. In addition, REDD1 and KLF15 were also considered as candidates of GR target genes (see the Supplemental Information available online).

Concerning KLF15, we showed, in gastrocnemius muscle and L6 myotubes but not in liver, that KLF15 mRNA and protein expression was induced in a GR-dependent manner (Figure 2A). The promoter region spanning from −4676 to +116 of KLF15 gene was not responsive to DEX; however, the activity of the region spanning −2108 to +1331 was induced by DEX, and

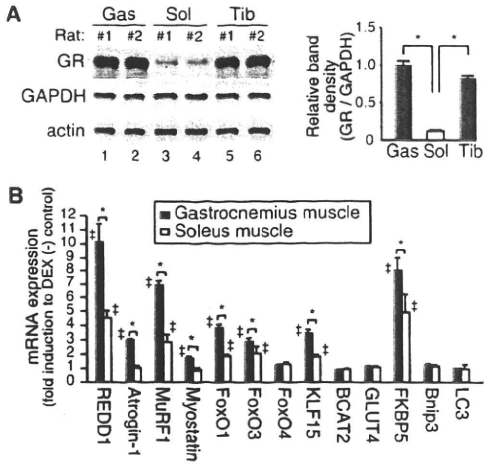

Figure 1. GR Protein Expression and Glucocorticoid-Dependent mRNA Expression of Atrophy-Related Genes in Rat Skeletal Muscles

(A) GR protein levels in rat gastrocnemius (Gas), soleus (Sol), and tibialis anterior (Tib). Left, representative immunoblots. Right, quantified protein levels of GR relative to GAPDH (n = 9).

(B) Induction of mRNA levels of atrophy-related genes by dexamethasone (DEX). Expression levels of the indicated mRNA in the muscles from rats 3 hr after intraperitoneal injection with DEX were assessed in quantitative RT-PCR (qRT-PCR). Results are shown as fold induction to vehicle-treated rats (n = 6).

(A and B) Error bars show SD. $^{*}p < 0.05$, $^{\ddagger}p < 0.05$ versus vehicle-treated rats.

this induction was inhibited by a GR antagonist RU486. The deletion and mutational analyses of KLF15 promoter indicated that both upper GRE1 and lower GRE2 sites were functional (Figures 2B and 2C). The transient transfection assays using the reporter constructs conveying these minimal GRE sites clearly showed that each GRE is independently functional (Figure 2D). A chromatin immunoprecipitation (ChIP) assay revealed that both GRE-like sequences were targeted by GR and that RNAPII was incorporated onto the coding region of KLF15 gene in the presence of DEX in L6 cells (Figure 2E). We also confirmed the DEX-dependent recruitment of endogenous GR onto the KLF15 promoter in a skeletal muscle-specific manner in vivo (Figure 2F). Similarly, we identified the functional GRE on the REDD1 promoter region and confirmed REDD1 as a GR target gene as well (Figure S1).

KLF15 Transactivates atrogin-1 and MuRF1 Genes

Next, we studied the alteration in the gene expression profile after the direct injection of a KLF15-expressing adenovirus into the rat tibialis anterior muscle. The exogenous expression of KLF15 increased KLF15 protein levels by approximately 5-fold (Figure 3A) and significantly induced mRNA expression of its target gene BCAT2 as anticipated (Figure 3B). Moreover, mRNA expression of atrogin-1, MuRF1, FoxO1, and FoxO3 was stimulated by KLF15 (Figure 3B). We then focused on atrogin-1 and MuRF1 and asked whether the DEX-mediated induction of their mRNA expression was dependent on KLF15. For that purpose, we tested the effect of knocking down the expression of GR or KLF15 on mRNA expression of KLF15, atrogin-1, and MuRF1 as well as another GR target gene REDD1 as a control. In L6 myoblasts, GR knockdown diminished the DEX-dependent mRNA induction of all of these GR target genes. However, KLF15 knockdown affected that of atrogin-1 and MuRF1 but not REDD1 (Figure 3C). These results strongly indicate the critical involvement of the GR-KLF15 cascade in the DEX-mediated upregulation of atrogin-1 and MuRF1 gene expression. To address the role of KLF15 in the transcriptional regulation of atrogin-1 and MuRF1, we constructed luciferase reporter plasmids driven by the promoter of rat atrogin-1 or MuRF1, and tested the effect of the exogenous expression of KLF15 in L6 myoblasts. The expression of the reporter genes was upregulated in a KLF15-dependent manner (Figure 3D). Since the promoter regions of atrogin-1 and MuRF1 contain a number of putative KLF15 recognition sites, we performed ChIP analyses; both promoters had multiple KLF15 binding sites and some of them were located in the proximity of FoxO binding sites and GRE (Figure 3E), and at least one of these KLF15 sites of each promoter recruited KLF15 in a DEX-dependent manner in vivo as well (Figure 3F). Note that atrogin-1 and MuRF1 were originally identified as FoxO target genes (Sandri et al., 2004; Waddell et al., 2008) and that KLF15 induced FoxO mRNA expression (Figure 3B). Indeed, the combination of KLF15 and FoxO significantly enhanced the promoter activity of atrogin-1 and MuRF1 when compared to their individual effects (Figure 3G). Moreover, the direct injection of the adenovirus expressing constitutively active FoxO1 or KLF15 significantly increased atrogin-1 and MuRF1 mRNA expression, and the expression of both resulted in synergistic or additive effects in tibialis anterior (Figure 3H). Therefore, it is likely that KLF15 and FoxO transcription factors cooperatively upregulate the expression of atrogin-1 and MuRF1 genes.

GR-KLF15 Axis Modulates BCAA Metabolism and mTOR Activity

Next, we studied the effects of glucocorticoids, GR, and KLF15 on BCAT2 and BCAA catabolism in skeletal muscle cells. In gastrocnemius muscle, mRNA expression of KLF15 preceded that of BCAT2 after treatment with DEX (Figure 4A). Overexpression of KLF15 increased the BCAT2 promoter-luciferase reporter activity (Figure 4B). Moreover, DEX-induced BCAT2 promoter activation was inhibited by either RU486 or siKLF15 (Figure 4C), indicating that KLF15 is mandatory for GR-mediated BCAT2 gene activation. BCAT2 enzyme activity was stimulated by DEX, and this effect was abolished in the presence of RU486 (Figure 4D). In tibialis anterior muscle and L6 myotubes, the adenovirus-mediated exogenous expression of KLF15 significantly induced BCAT2 enzyme activity even in the absence of DEX (Figure 4E).

The measurement of intracellular amino acid levels clearly revealed the accelerated catabolism of BCAA by KLF15 in myotubes; the exogenous expression of KLF15 decreased the levels of Val, Leu, and Ile, with a reciprocal increase in Ala and Glu without significant alterations in, for example, Gly, Trp, Gln, Tyr, and Phe, in L6 myotubes (Figure 4F). Amino acids, especially BCAA, are believed to activate mTOR and to increase in association with Rheb-mTOR (Sancak et al., 2010). We showed that overexpression of KLF15 in C2C12 myotubes suppressed mTOR activity as demonstrated by the decrease in the phosphorylated form of S6K1. Moreover, mTOR activity was complemented by the addition of excess BCAA (Figure 4G). Of note,

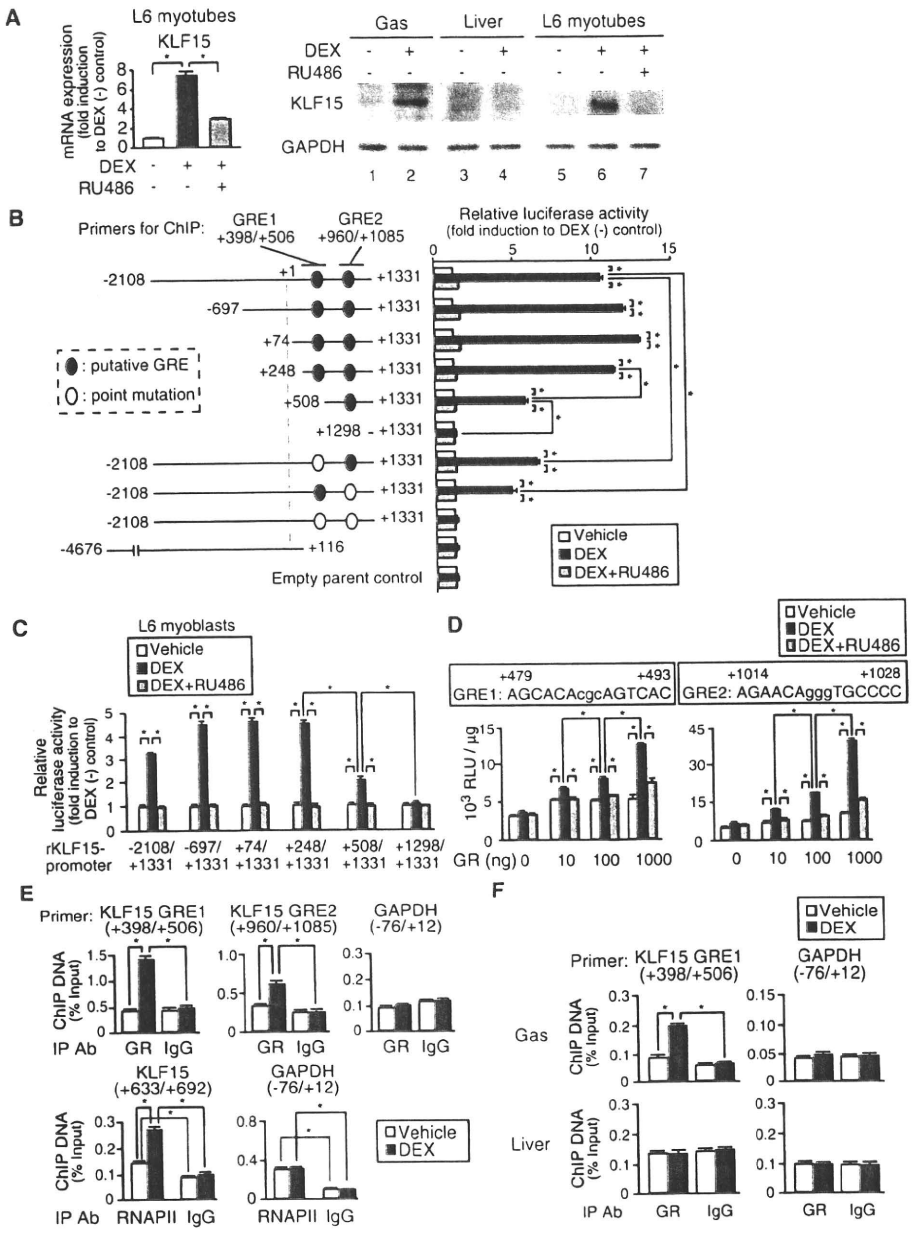

Figure 2. Identification of KLF15 as a Direct GR Target Gene

(A) GR-dependent mRNA (left) and protein (right) expression of KLF15 in L6 myotubes treated with DEX and RU486 for 6 hr and in DEX-treated rat gastrocnemius (see legend for Figure 1B).

(B) Identification of GREs in rat KLF15 promoter. Left, schematic of rat KLF15 promoter-luciferase reporter constructs. Positions of the primers for chromatin immunoprecipitation (ChIP) in (E) and (F) are shown. Right, GR-dependent activation of rat KLF15 promoter-reporter genes. COS-7 cells were transfected with the reporter constructs and 100 ng of GR expression plasmid and treated with DEX and RU486 for 18 hr.

(C) GR-dependent activation of rat KLF15 promoter-reporter genes in L6 myoblasts treated with DEX and RU486 for 18 hr.

(D) GR-dependent activation of reporter genes containing KLF15 promoter GREs. L6 myoblasts were transfected with the luciferase reporter constructs containing the GREs from rat KLF15 with GR expression plasmid and treated with DEX and RU486 for 18 hr.

(E) DEX-dependent recruitment of GR and RNAPII onto rat KLF15 gene. L6 myotubes treated with 1 µM DEX for 2 hr were subjected to ChIP.

(F) Skeletal muscle-specific recruitment of GR onto rat KLF15 gene by DEX. DEX-treated rat gastrocnemius (Gas) and liver (see legend for Figure 1B) were subjected to ChIP.

(A–F) Error bars show SD (n = 5). *p < 0.05.

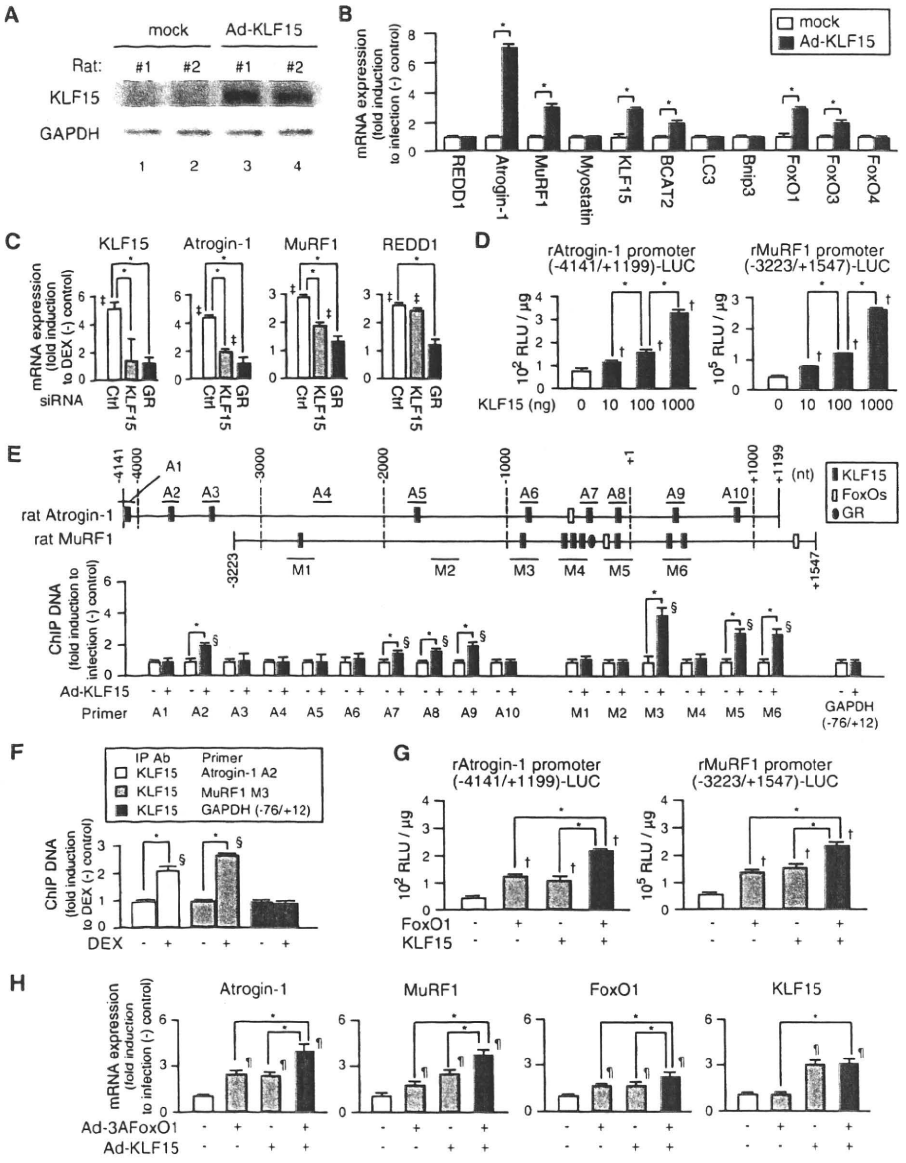

Figure 3. Transcriptional Regulation of Atrogenes by KLF15 and FoxOs

(A and B) KLF15-dependent mRNA expression of atrophy-related genes. Recombinant adenovirus Ad-KLF15 was infected to rat tibialis anterior for 7 days. (A) Immunoblot detection of ectopic KLF15. (B) qRT-PCR.

(C) Effects of knockdown of KLF15 or GR on DEX-dependent mRNA expression of atrophy-related genes. L6 myoblasts were transfected with control siRNA, siRNA against KLF15, or siRNA against GR and treated with DEX for 18 hr.

(D) KLF15-dependent activation of rat atrogin-1 (left) and MuRF1 (right) promoter-reporter genes in L6 myoblasts.

(E) Mapping of the binding sites for KLF15, FoxOs, and GR in rat atrogin-1 and MuRF1 promoters. Top, putative binding sites identified in in silico promoter analysis (see the Experimental Procedures and the Supplemental Information). Bars indicate the positions of the primers for ChIP. Bottom, recruitment of KLF15 onto rat atrogin-1 and MuRF1 promoters. L6 myotubes were infected with Ad-KLF15 for 5 days and subjected to ChIP using anti-KLF15 antibody.

(F) DEX-dependent recruitment of KLF15 onto rat atrogin-1 and MuRF1 promoters in rat gastrocnemius (see Figure 1B).

(G and H) Effects of FoxOs and KLF15 on rat atrogin-1 and MuRF1 promoter-reporter gene expression in L6 myoblasts (G) and on atrogin-1 and MuRF1 mRNA expression in rat tibialis anterior (H). (G) Luciferase assay of L6 myoblasts transfected with the reporter constructs with or without FoxO1 and/or KLF15 expression plasmids. (H) qRT-PCR analysis of rat tibialis anterior expressing ectopic KLF15 and/or constitutive active FoxO1 (3AFoxO1) for 3 days.

(B–H) Error bars show SD (n = 5). *$p < 0.05$, †$p < 0.05$ versus vehicle-treated cells, ‡$p < 0.05$ versus mock-transfected cells, §$p < 0.05$ versus ChIP with normal IgG, ¶$p < 0.05$ versus mock-infected rats.

the diameter of C2C12 myotubes was shortened by KLF15 and rescued by BCAA (Figure 4G). Moreover, exogenous KLF15 reduced mTOR activity with fiber type-independent atrophy in the tibialis anterior muscle (Figure 4H). Taken together, these data indicate that KLF15 is a liaison molecule for GR in the induction of atrogenes and the acceleration of BCAA catabolism and mTOR repression to decrease myofiber size.

mTOR Affects GR-Mediated Transcriptional Regulation

Since little is known about how glucocorticoid-mediated catabolic signal transduction is shut off, we next examined the effects of mTOR blockade using rapamycin on GR-mediated gene expression in L6 myotubes. Surprisingly, rapamycin significantly enhanced the DEX-induced mRNA expression of a number of GR target genes, including REDD1, atrogin-1, MuRF1, KLF15, FoxOs, and FKBP5 (Figure 5A). These results strongly suggest that mTOR blockade selectively enhances mRNA expression of GR target genes, i.e., mTOR activation appears to have a negative impact on GR-mediated gene expression. To further address this negative modulation of GR function by mTOR, we performed transient transfection assays using GR-responsive KLF15 promoter-Luc and GRE-Luc reporter genes in L6 myoblasts. A constitutively active mutant of Rheb, RhebS16H, which autonomously activates mTOR, repressed DEX-mediated reporter gene activation, and rapamycin inhibited these negative effects of RhebS16H (Figure 5B). Moreover, a major endogenous mTOR activator IGF-1 slightly enhanced S6K1 phosphorylation and did not affect DEX-induced GRE-Luc expression when cultured in amino acid-rich media. In clear contrast, in amino acid-deprived media, DEX-dependent induction of GRE-Luc was approximately doubled, and IGF-1 strongly phosphorylated S6K1 and suppressed DEX-induced GRE-Luc expression (Figure 5C). These results indicated that, regardless of the upstream pathways for mTOR activation, endogenous GR activity is negatively controlled by mTOR in L6 myoblasts.

We then asked the underlying mechanisms for mTOR-mediated GR suppression. To test whether mTOR-mediated GR repression is via global protein synthesis downstream of mTOR, we examined luciferase mRNA expression in transient transfection assay using GRE-Luc reporter plasmid in the presence or absence of the protein synthesis inhibitor cycloheximide. Cycloheximide did not influence on either GR-mediated GRE activation or BCAA-mediated GR suppression (Figure 5D). Therefore, BCAA inhibits the transcriptional effects of GR via mTOR activation but not via de novo protein synthesis. Immunoblotting using L6 myotubes revealed that GR protein levels were unaltered in the presence of DEX, BCAA, or rapamycin. Treatment with DEX clearly promoted the nuclear translocation of GR, and such a process was not affected by BCAA or rapamycin (Figure 5E). Concerning the promoter regions spanning the putative GREs in KLF15 and REDD1, DEX-induced GR recruitment was significantly enhanced by rapamycin, suggesting that mTOR negatively influences the access of GR to these promoters. Such an enhancement of GR promoter binding by rapamycin was paralleled by RNAPII recruitment onto the coding regions of KLF15 and REDD1 (Figure 5F). Thus, cellular mTOR activity negatively modulates GR transcriptional function, most possibly by altering the intranuclear behavior of GR. We finally examined the effect of constitutive mTOR activation by studying the impact of adeno-associated virus-driven RhebS16H expression on S6K1 activity and the gene expression profile of the tibialis anterior muscle from DEX-treated rats. RhebS16H-injected muscle had elevated levels of S6K1 phosphorylation and significant decreases in the induction response to DEX of a number of glucocorticoid-inducible genes, including REDD1, atrogin-1, MuRF1, FoxOs, KLF15, and FKBP5, when compared to mock-injected muscle (Figures 5G and 5H).

mTOR Activation Attenuates Glucocorticoid-Induced Muscle Atrophy

It should be noted that numerous studies examined the effects of BCAA on mTOR activity in glucocorticoid-induced atrophy models with conflicting results, the reason for which might be variations in the protocols used in those in vivo studies (Menconi et al., 2007; Schakman et al., 2008). We showed that the bolus administration of a BCAA cocktail via a gastric tube just before the peritoneal injection of DEX (Supplemental Information) resulted in sufficient and reproducible mTOR activation in the gastrocnemius muscle; the phosphorylated form of S6K1 was increased at 30 min after BCAA administration and returned to the baseline level after 90–180 min, even in the presence of DEX (Figure 6A). We then tested the effects of DEX, BCAA, and rapamycin on the protein levels and phosphorylation status of mTOR and its downstream effectors S6K1 and 4E-BP1 as well as Akt, the upstream activator of mTOR, in the rat glucocorticoid-induced atrophy model (5 day intraperitoneal DEX administration, see the Supplemental Information). In GR-rich gastrocnemius muscle, treatment with DEX suppressed the phosphorylation of S6K1 and 4E-BP1, without a significant alteration in p-Akt, indicating that DEX inhibited mTOR function in an Akt-independent fashion in this model. In clear contrast, in either the soleus muscle or liver, DEX treatment did not affect mTOR activity. When BCAA was supplemented, the levels of p-S6K1 and p-4E-BP1 were efficiently restored. Of note, rapamycin canceled these effects of BCAA (Figure 6B). In this model, BCAA administration suppressed the glucocorticoid-induced expression of REDD1, atrogin-1, MuRF1, KLF15, FoxOs, and FKBP5 mRNA (Figure 6C), and there was a decrease in GR recruitment onto the promoters of KLF15, REDD1, MuRF1, and FKBP5 (Figure 6D). BCAA administration also repressed the expression of BCAT2, GLUT4, Bnip3, and LC3 mRNA, and treatment with rapamycin inhibited the effects of BCAA (Figure 6C). In contrast, in the soleus muscle, treatment with DEX alone or DEX plus BCAA only marginally influenced mTOR activity and the gene expression profile, if at all (Figures 6B and 6C).

In this glucocorticoid-induced muscle atrophy rat model, there was a decrease in the body weight of the DEX, DEX plus BCAA, and DEX plus BCAA plus rapamycin groups (Figure 7A). The DEX plus BCAA group revealed a significant restoration of muscle strength as determined by a grip test and the weight of the gastrocnemius muscle when compared with DEX group (Figures 7B and 7C). Histological examination of the gastrocnemius muscle demonstrated typical type II fiber-dominant atrophy in the DEX group; however, the DEX plus BCAA group showed less impairment in the gastrocnemius muscle that was represented by the prevention of type II fiber loss. Semiquantitative analysis using cross-sectional area (CSA) analysis of myofibers strongly supported this notion; the leftward shift in myofiber size

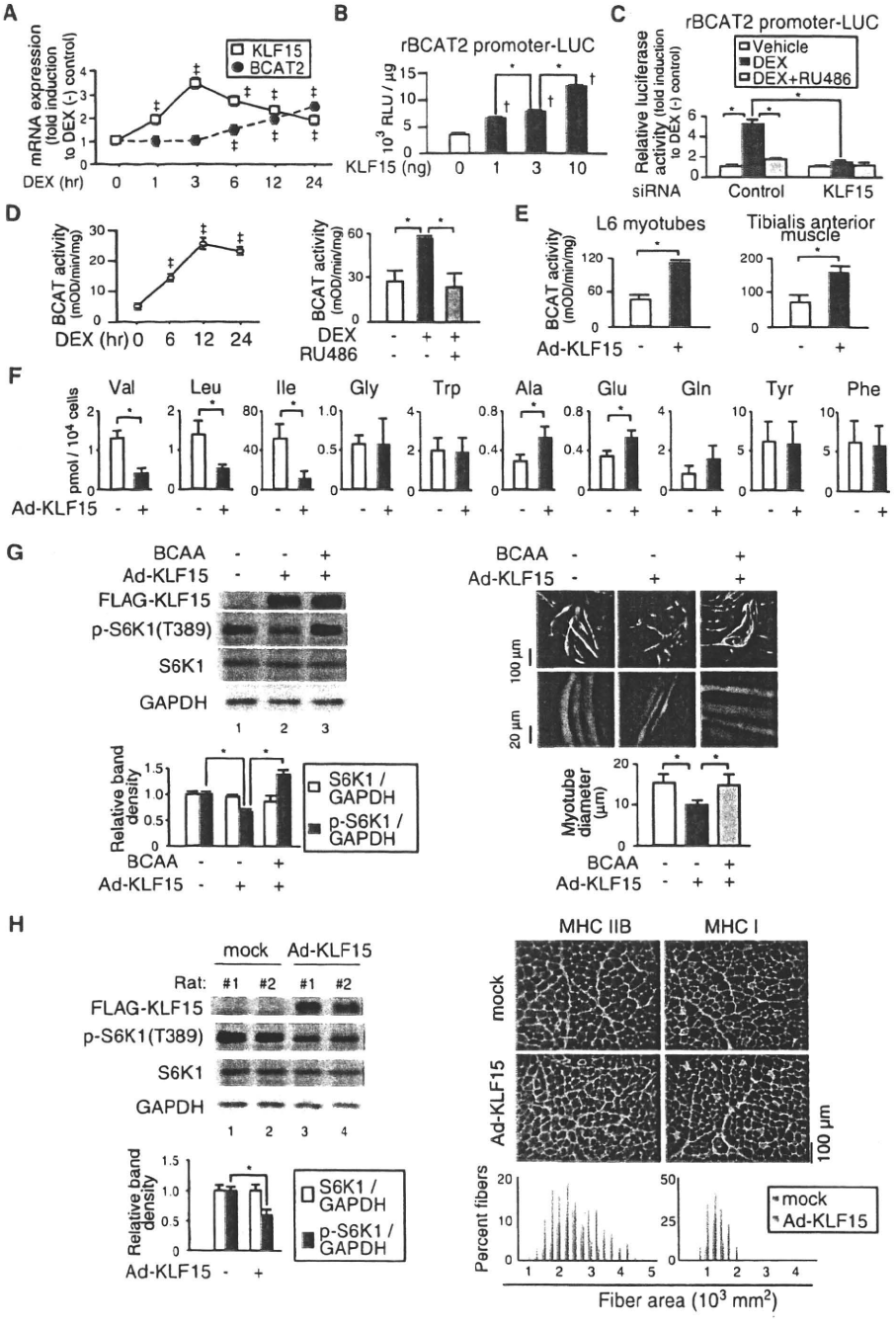

Figure 4. KLF15-Mediated Modulation of BCAA Metabolism and Myofiber Size

(A) Time course of mRNA expression of KLF15 and BCAT2 in rat gastrocnemius after intraperitoneal DEX-injection (n = 5).

(B) KLF15-dependent activation of rat BCAT2 promoter-reporter gene expression in L6 myoblasts (n = 5).

(C) Diminished GR-dependent activation of rat BCAT2 promoter-reporter gene by knockdown of KLF15 in L6 myoblasts (n = 5).

(D) GR-dependent activation of BCAT activity in rat gastrocnemius. Rats were treated with RU486 and/or DEX for the indicated time periods (left) or 6 hr (right) and subjected to BCAT activity measurement as described in the Supplemental Information (n = 5).

(E) KLF15-dependent activation of BCAT activity (n = 5).

(F) Effects of ectopic KLF15 on intracellular amino acid concentrations. L6 myotubes were infected with Ad-KLF15 for 2 days, cultured in amino acid-deprived DMEM for 24 hr, and subjected to quantification of intracellular amino acids as described in the Supplemental Information (n = 3).

(G) Effects of KLF15 and BCAA on mTOR activity and myotube diameter. C2C12 myotubes were infected with GFP-expressing adenovirus and Ad-KLF15 for 2 days and further cultured in amino acid-deprived DMEM supplemented with or without 10 mM BCAA cocktail for 24 hr. Left, representative immunoblots

was observed in the DEX group, but not in the DEX plus BCAA group. In contrast, there was no significant difference in the size of slow type I fibers among the three treatment groups. Moreover, the therapeutic effects of BCAA were inhibited by rapamycin (Figures 7B–7E). Therefore, we conclude that the administration of BCAA elicits mTOR activation and intervenes in GR-dependent catabolic transcriptional regulation to ameliorate DEX-induced muscle atrophy.

DISCUSSION

In skeletal muscle, we suggested that GR activates a secondary transcription network driven by KLF15; that the promoter regions of atrogin-1 and MuRF1 contain KLF15 binding sites as well as those of FoxOs; and that KLF15 induces the expression of these atrogenes. Although the molecular mechanism remains elusive, the functional cooperativity of GR, FoxOs, and KLF15 in the expression of the atrogenes may represent the molecular basis for the involvement of GR in muscle atrophy associated with a number of pathological conditions including diabetes and sepsis. From the metabolic viewpoint, these GR-driven transcriptional cascades appear to be relevant for providing rapid and integrated cues toward muscle breakdown and nutrient supply from muscle to other organs, i.e., to the liver, under stressful conditions associated with excess levels of glucocorticoids.

BCAT2 catalyzes the initial step for BCAA degradation, and BCAT2 activity is a critical determinant of cellular BCAA content in skeletal muscle; mice with systemic inactivation of BCAT2 gene are reported to have approximately ten times or higher concentrations of plasma BCAA (She et al., 2007). We demonstrated that BCAA content was decreased with a reciprocal increase in alanine levels in L6 myotubes after the exogenous expression of KLF15 (Figure 4F). Although it is generally known that BCAA is supplied via protein breakdown during skeletal muscle atrophy (Wagenmakers, 1998; Yu et al., 2010), it was reported that net increase in muscle BCAA concentrations after glucocorticoid treatment (~150% increase compared to control) were strikingly lower than those of diabetic rats (~400% increase compared to control) (Aftring et al., 1988; Hundal et al., 1991). This difference in BCAA concentrations is most likely to be due to increased BCAT2 activity in glucocorticoid-treated rats. The glucocorticoid-driven GR-KLF15-BCAT2 axis may negatively modulate the intracellular availability of BCAA and result in a negative impact on mTOR function in skeletal muscle. Indeed, exogenous KLF15 increased mRNA expression of the atrogenes and BCAT2 and decreased mTOR activity and BCAA concentrations in cultured myotubes (Figures 4E–4G). Moreover, the introduction of KLF15 decreased myofiber size in cultured myotubes and caused atrophy in the tibialis anterior muscle, even in the absence of glucocorticoids (Figures 4G and 4H). Therefore, we may conclude that KLF15 is a crucial GR target gene acting as a catabolic modulator of skeletal muscle.

In addition to the KLF15-BCAT2 axis, it should be noted that a number of glucocorticoid-induced products can repress mTOR activity in skeletal muscle cells. Among others, myostatin (Ma et al., 2001; Gilson et al., 2007) and REDD1 (Figure S1) (DeYoung et al., 2008) are direct targets of GR. Moreover, atrogin-1 was recently reported to inhibit S6K1 activity via eIF3f (Csibi et al., 2010). Therefore, it is likely that the mTOR system is negatively regulated by a variety of factors in the presence of excess glucocorticoids in a distinct fashion. Given that the glucocorticoid-GR axis is a major catabolic regulator for homeostatic control (Munck et al., 1984), this multimodal repression of mTOR via the GR axis appears to be rational. In any case, this type of negative mTOR modulation is not reported in other types of muscle atrophy, and may be a striking feature in glucocorticoid-induced muscle atrophy. Interestingly, muscle-specific inactivation of mTOR was reported to exacerbate the myopathic features of type I and type II fiber-rich muscles in a distinct fashion; type I fiber-rich muscles showed prominent dystrophic features with less impact on muscle mass and CSA compared to type II fiber-rich muscles, and a decrease in muscle mass and CSA are characteristic of type II fiber-rich muscles with less dystrophic appearance (Bentzinger et al., 2008; Risson et al., 2009). Therefore, we speculate that type II fiber-rich glycolytic muscles have an evolutionally preserved role for the storage of nutrients under the control of the glucocorticoid-GR axis and that the GR-triggered gene expression program is a purposeful and efficient compensatory mechanism for nutrient supply from those muscles.

An important question is how the GR-driven proteolytic cascades can be shut down when necessary in skeletal muscle. We clearly demonstrated that mTOR activation negatively modulated GR-mediated transcription. Given that the effect of mTOR is rapamycin sensitive, the involvement of mTORC1 is strongly indicated in this interaction. The role of the mTOR pathway in the determination of glucocorticoid sensitivity has not yet been highlighted, except in certain hematologic malignancies (Beesley et al., 2009; Gu et al., 2008; Yan et al., 2006a). It was postulated that the treatment of cultured cells with FK506 or rapamycin enhances glucocorticoid-inducible reporter gene expression, most possibly via their interaction with heat shock proteins and the promotion of the ligand-dependent nuclear entry of GR (Ning and Sanchez, 1993). In contrast, we documented that rapamycin, without any alteration in the cytoplasmic-nuclear distribution of GR, increased GR recruitment onto the promoter (Figures 5E and 5F), and these effects were not reproduced by FK506 (data not shown).

and quantified band densities of S6K1 and p-S6K1(T389) relative to GAPDH (n = 5). Right, representative fluorescent microscopic images of the myotubes and quantified diameters of the myotubes (500 < n < 510).

(H) Effects of ectopic KLF15 expression on mTOR activity and myofiber cross-sectional area (CSA) in rat tibialis anterior. Left, representative immunoblots and quantified band densities (n = 5). Right, immunostaining for type IIB myosin heavy chain (MHC IIB, red in left photographs), type I myosin heavy chain (MHC I, red in right photographs), and type IV collagen (green) of transverse cryosections. CSA distribution of MHC IIB fibers (left) and MHC I fibers (right) are presented as frequency histograms (500 < n < 510).

(A–H) Error bars show SD. $^{*}p < 0.05$, $^{\dagger}p < 0.05$ versus vehicle-treated rats. $^{\dagger}p < 0.05$ versus mock-transfected cells.

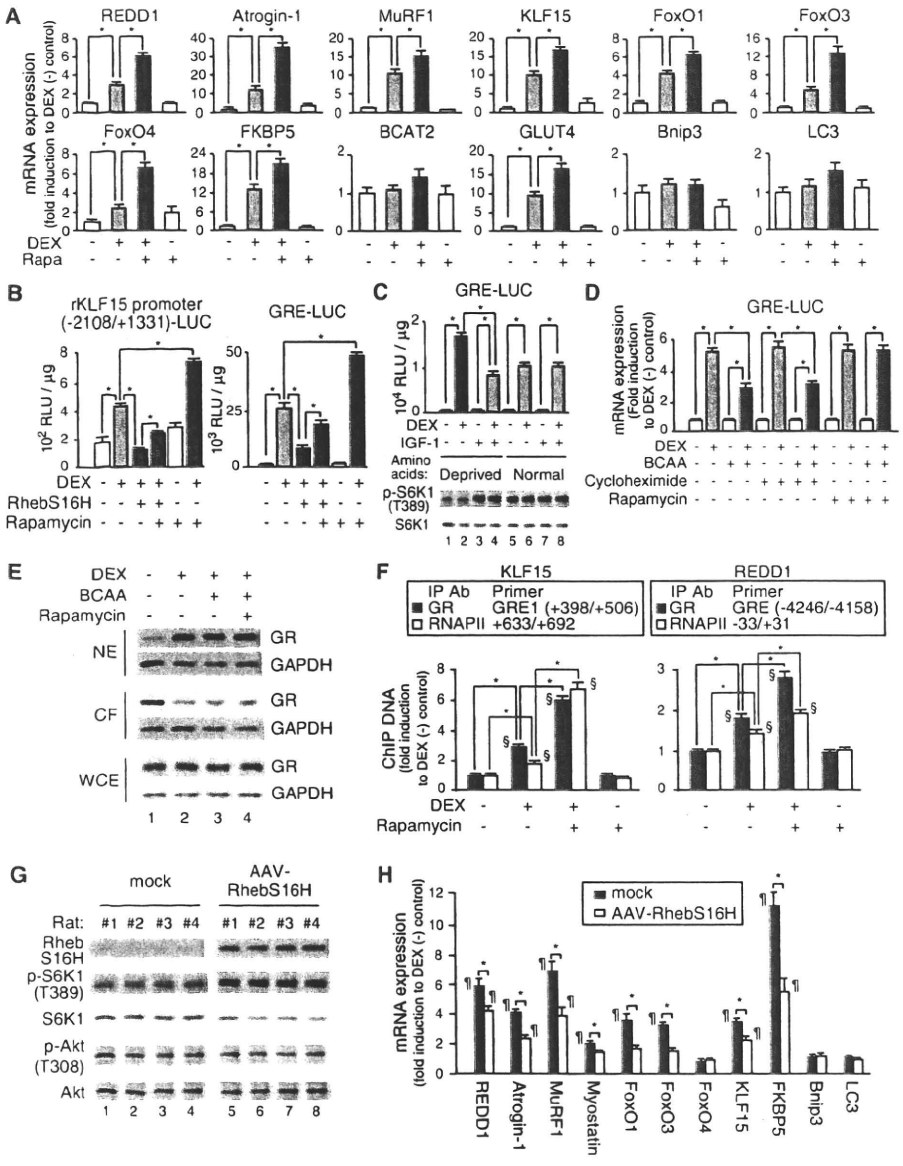

Figure 5. Negative Regulation of GR-Mediated Transcription by mTOR

(A) qRT-PCR analysis of L6 myotubes treated with DEX and rapamycin (Rapa) for 24 hr.

(B) Attenuation of GR-dependent reporter gene expression by mTOR. L6 myoblasts were transfected with rKLF15 promoter-LUC or GRE-LUC, with or without the expression plasmid for a constitutive active Rheb (RhebS16H), and treated with DEX and rapamycin for 18 hr.

(C) Effects of IGF-1 on mTOR activity and GR-dependent reporter gene expression. L6 myoblasts were transfected with GRE-LUC and cultured in amino acid-deprived DMEM (lanes 1–4) or normal DMEM (lanes 5–8) in the presence or absence of IGF-1 and/or DEX for 9 hr. Top, luciferase activities. Bottom, representative immunoblots.

(D) Effects of DEX, BCAA, cycloheximide, and rapamycin on GR-dependent reporter gene expression. L6 myoblasts were transfected with GRE-LUC and cultured in amino acid-deprived DMEM in the presence or absence of 10 mM BCAA cocktail, cycloheximide, rapamycin, and DEX for 6 hr.

(E) Effects of DEX, BCAA, and rapamycin on protein levels and subcellular localization of GR. L6 myotubes were cultured in amino acid-deprived DMEM in the presence or absence of DEX, 10 mM BCAA cocktail, and rapamycin for 30 min. Representative immunoblots of the nuclear extracts (NE), cytoplasmic fractions (CF), and whole-cell extracts (WCE) are shown (n = 3).

(F) Effects of rapamycin on DEX-dependent recruitment of GR onto target gene promoters. L6 myotubes were treated with 1 μM DEX and rapamycin for 2 hr (for KLF15) or 20 min (for REDD1) and processed for ChIP assays.

(G and H) Effects of ectopic expression of RhebS16H on mTOR activity and DEX-mediated mRNA expression. AAV-RhebS16H was infected to rat tibialis anterior for 7 days. (G) Representative immunoblots (n = 7). (H) qRT-PCR analysis of the muscles from the rats 6 hr after intraperitoneal injection with DEX.

(A–D, F, and H) Error bars show SD (n = 5). *$p < 0.05$, §$p < 0.05$ versus ChIP with normal IgG, ¶$p < 0.05$ versus vehicle-treated rats.